OXIDATIVE DISSOLUTION UNDER THE CHANNEL LEADS GEOMORPHOLOGICAL EVOLUTION AT THE SHALE HILLS CATCHMENT

PAMELA L. SULLIVAN*,a,†, SCOTT A. HYNEK*, XIN GU*, KAMINI SINGHA**, TIMOTHY WHITE*, NICOLE WEST*,b, HYOJIN KIM*, BRIAN CLARKE*, ERIC KIRBY***, CHRISTOPHER DUFFY§, and SUSAN L. BRANTLEY*

ABSTRACT. The hydrologic connectivity between hillslopes and streams impacts the geomorphological evolution of catchments. Here, we propose a conceptual model for hydrogeomorphological evolution of the Susquehanna Shale Hills Critical Zone Observatory (SSHCZO), a first-order catchment developed on shale in central Pennsylvania, U.S.A. At SSHCZO, the majority of available water (the difference between incoming meteoric water and outgoing evapotranspiration) flows laterally to the catchment outlet as interflow, while the rest is transported by regional groundwater flow. Interflow, shallow hillslope flow, is limited to the upper 5 to 8 m of highly fractured bedrock, thought to have formed during periglacial conditions in the late Pleistocene. In contrast, groundwater flowpaths are influenced by the primary permeability of the varying stratigraphic units. Both flowpaths respond to weathering-related secondary permeability. O_2-rich interflow mixes with deep O_2-poor groundwater under the catchment outlet at depths of 5–8 m. Penetration of this oxygenated interflow under the valley results in pyrite oxidation, release of sulfuric acid, dissolution of minerals, and weakening of bedrock. This is hypothesized to enhance channel incision and, in turn, to promote drainage of deep groundwater from the ridges. Drainage subsequently lowers the catchment water table, advancing the cascade of reactions that produce regolith. Weathering in the catchment is characterized by both sharp and diffuse reaction fronts. Relatively sharp fronts (pyrite, carbonate) mark where vertical, unsaturated flow changes to horizontal, saturated flow, while diffuse fronts (illite, chlorite, feldspar) mark where flow is largely vertical and unsaturated. According to this model, catchment morphology reflects subsurface pyrite reactions due to mixing of interflow and groundwater flow under the valley floor that ultimately results in clay weathering and regolith production nearer the land surface.

Keywords: Reaction fronts, weathering, regolith, hydrogeology, shale

INTRODUCTION

Meteoric water dissolves and precipitates minerals as it interacts with rock along flowpaths in the subsurface of catchments. Differences among reaction kinetics and solubilities promote preferential losses and gains of elements, which then affect the porosity and permeability of the protolith (unweathered bedrock) (Strumm, 1997; Brantley, 2008; Brantley and White, 2009; Graham and others, 2010; Jin and others, 2011a; Maher, 2011; Brantley and others, 2016). The goal of this paper is to link observations of regolith chemistry to flowpaths in the subsurface of one small catch-

* Earth and Environmental Systems Institute, and Department of Geosciences, The Pennsylvania State University, University Park, Pennsylvania 16802
** Department of Geology and Geologic Engineering, Colorado School of Mines, Golden, Colorado 80401
*** College of Earth, Ocean and Atmospheric Sciences, Oregon State University, Corvallis, Oregon 97331
§ Department of Civil and Environmental Engineering, The Pennsylvania State University, University Park, Pennsylvania 16802
a Current Affiliation Department of Geography and Atmospheric Science, University of Kansas, Lawrence, Kansas 66045
b Current Affiliation Department of Earth and Atmospheric Sciences, Central Michigan University, Mt. Pleasant, Michigan 48859
† Corresponding author: plsullivan@ku.edu

ment where geochemical and geomorphological evolution can be related: the Susquehanna Shale Hills Critical Zone Observatory (SSHCZO). In the catchment, the depth interval over which a mineral concentration changes from that of the parent protolith to that of regolith is referred to as the mineral reaction front (Lichtner, 1988; White and Brantley, 1995; Brantley and others, 2007; Lebedeva and others, 2007; Brantley and Lebedeva, 2011). As has been documented in other catchments (Chigira, 1990; Chigira and Oyama, 1999; Drake and others, 2009), we observe a sequence of reaction fronts that are nested in the subsurface of the catchment, with overlap under the valley. We explore how the downward propagation of nested reaction fronts into the subsurface can open porosity and enhance permeability, and thus can increase the rate of water transmittance. To unravel the interplay between water flow and development of nested reaction fronts in the subsurface, we discuss bulk geochemical analyses from nine boreholes and groundwater geochemistry and age tracers from 25 wells across the SSHCZO. We also show how the underlying porosity, permeability and structure (strike and dip) of the protolith contribute to the catchment hydrology.

The SSHCZO is a well-studied first-order catchment, which is underlain by the shale-dominated Rose Hill Formation in central Pennsylvania (U.S.A.). Recent measurements of [10]Be (West and others, 2013; West and others, 2014) and U-series isotopes (Ma and others, 2013) at Shale Hills indicate the ridgetop soil production rates are within error of the soil erosion rates, leading to near steady-state conditions. West and others (2014) also observed that the hillslope mass fluxes in the augerable soils increased linearly with downslope position, providing a compelling argument for relatively steady lowering of both channel and ridgetop.

Geochemical evidence from boreholes drilled at two locations in Shale Hills revealed depletion of carbonate minerals down to depths roughly coincident with the regional water table: 20 to 25 mbls (meters below the land surface) at the ridge and ~2 mbls at the valley floor (Brantley and others, 2013). In addition, pyrite was observed to be depleted to the regional water table beneath the ridge and to about 6 m deeper than the regional water table under the valley. Such reaction fronts have been inferred at other locations worldwide (for example, Singh and others, 1982; Hercod and others, 1998; Drake and others, 2009; see other instances in a review by Brantley and others, 2013). In areas where a changing climate is driving the water table to greater depths, these fronts may be deepening with time (Manning and others, 2013).

At the SSHCZO, Jin and others (2011) referred to subsurface material that was depleted in pyrite and carbonate as "saprock" to indicate that it had most of the physical attributes of unaltered bedrock but showed some chemical and/or physical alteration. In the saprock, weathering was inferred to have created additional pore space and fractures compared to unaltered bedrock based on immersion and neutron scattering measurements (Jin and others, 2010; Jin and others, 2011). Soil moisture and hydrologic observations have also documented preferential horizontal water flowpaths at various depths within meters of the land surface (Lin, 2006; Lin and others, 2006; Lin and Zhou, 2008). Preferential flowpaths have been inferred to be roughly coincident with plagioclase (~5 mbls on ridgetops) and illite reaction fronts (~0.4 mbls on the ridgetops), respectively. The plagioclase reaction begins in a surficial zone of high density fracturing (5–8 mbls) that has been attributed to periglacial processes during the late Pleistocene and Last Glacial Maximum (LGM; Brantley and others, 2013; Sullivan and others, 2016). The illite reaction begins in this fractured layer but becomes important only in the zone of augerable regolith (0.3–3 m).

We use the term interflow to describe meteoric waters that flow through intermittently saturated zones down the hillslopes of the catchment above the regional water table. Such interflow has been inferred from soil moisture (Lin, 2006), water isotope

patterns (Jin and others, 2011; Thomas and others, 2013), and ground-penetrating radar measurements that are consistent with strong contrasts in regolith permeability roughly delineating the boundaries between the fractured zone and the augerable regolith (Guo and others, 2014; Zhang and others, 2014). Such interflow has also been observed or inferred in other catchments. For example, Bishop and others (1990, 2004) argued that contrasting zones of permeability explained the concentration-discharge behavior of solutes in a stream in northern Sweden, as the water that flows through each zone is inherently fingerprinted by distinct biogeochemical processes (for example, mineralogy).

Here, we propose a conceptual model for hydrogeochemical and geomorphological evolution of the catchment. We constrain the magnitudes of a few of the hydrologic and solute fluxes at the SSHCZO and consider these fluxes in the context of the hypothesis of nested reaction fronts. We also try to put the observations within a geomorphological context by relating to landscape processes such as chemical weathering (Lebedeva and others, 2010), throughflow of meteoric water (Maher, 2010), and fracturing (Molnar and others, 2007). The model explores the idea that the rate of channel incision governs the removal of water from the saturated zone in this small upland catchment and thus controls the rate of ridgetop weathering and erosion (Rempe and Dietrich, 2014). While Rempe and Dietrich emphasize that catchment geomorphic evolution is controlled by primary porosity and permeability of the protolith and the hydraulic gradient established through erosion-driven channel incision, we propose that the primary permeability structure is only a scaffold upon which the regolith forms, and we show that secondary permeability is the most important, direct control on meteoric water flowpaths, producing a hydrogeochemical feedback that enhances channel incision.

<center>study area</center>

The Susquehanna Shale Hills Critical Zone Observatory (SSHCZO) is a 7.9 ha V-shaped forested catchment that lies within the Valley and Ridge Physiographic Province of the Appalachian Mountains in central Pennsylvania. The catchment is generally oriented east-to-west, bisected by a first-order ephemeral stream and underlain by the Rose Hill Formation, a member of the Silurian Clinton Group. The overlying Keefer Sandstone, a prominent 1 to 10 m thick sandstone in central Pennsylvania also included in the Clinton Group, exists in the subsurface at the outlet of the catchment (fig. 1). Stratigraphic sections of the Rose Hill Formation exposed in the Shavers Creek and nearby Juniata River watersheds reveal that it is comprised primarily of shale with thin interbeds of limestone and sandstone in the upper half (Flueckinger, 1969; Cotter and Inners, 1986). Near the contact between the Rose Hill and the Keefer Sandstone which underlies the outlet of the Shale Hills catchment, the occurrence of limestone and sandstone interbeds within the Rose Hill Formation increases (fig. 1). Pristine Rose Hill Shale is dominantly comprised of quartz and the clay minerals illite and "chlorite", while plagioclase feldspar, pyrite and carbonate minerals (ankerite and calcite) are present in much lower concentrations (Jin and others, 2010). Here, "chlorite" is used to represent not only the mineral chlorite itself, but also the reaction products vermiculite and hydroxy-interlayered vermiculite.

The SSHCZO watershed experiences a humid-temperate climate: the 30-year averages for precipitation and temperature are 107 cm yr^{-1} and 10 °C, respectively (USC00368449 location, NOAA 2007). Approximately 54 m of relief separate the stream outlet from the highest ridge top point. Catchment hillslopes are characterized by gradients that range from 8 to 30 percent (West and others, 2013) and are classified into two main slope types: 1) abundant near-planar interfluve hillsides, and 2) infrequent but hydrologically important swales (hillslopes experiencing convergent
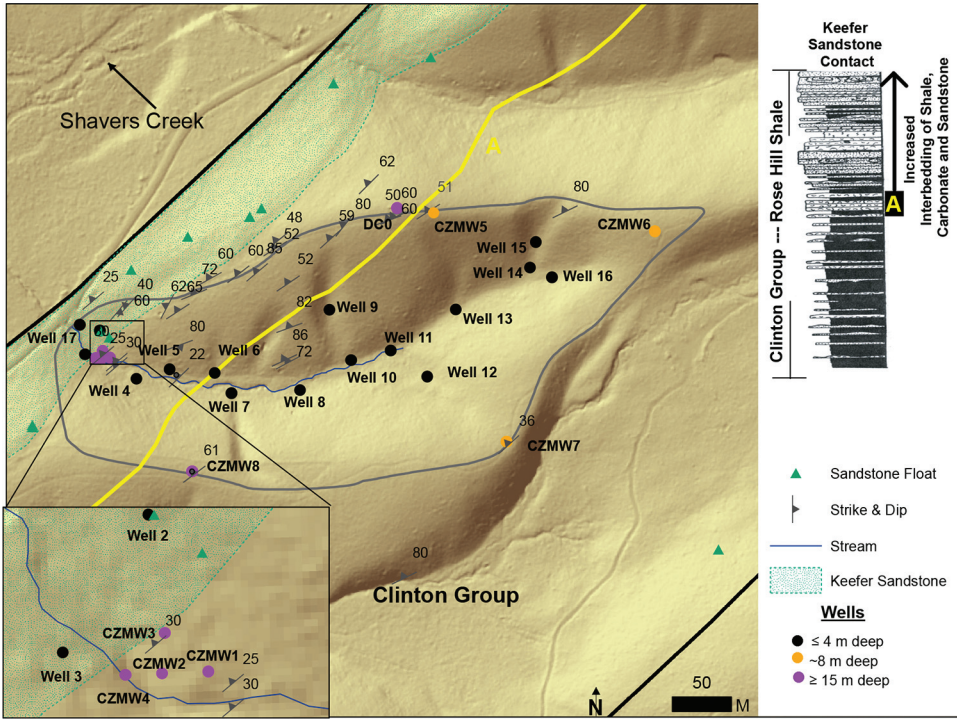
Fig. 1. Susquehanna Shale Hills CZO resides completely on the Rose Hill Shale Formation of the Clinton Group. The frequency of sandstone and limestone interbeds increases from the bottom in the Rose Hill Shale toward the top of this stratigraphic section, in other words the base of the Keefer Sandstone. The increase in interbeds is especially pronounced above the yellow line (marked A). A total of 25 groundwater wells and boreholes at SSHCZO were examined in this study. Location of sandstone fragments observed at land surface (float) are marked with triangles and strike and dip measurements are noted.

water and sediment flow). West and others (2013) also showed that the southern side of the catchment is steeper than the northern side.

The augerable regolith, referred to here as soil, at the SSHCZO is formed from shale colluvium or residuum. The soils include rock fragments that generally decrease in size and abundance and increase in fine-scale porosity upward toward the ground surface (Lin and others, 2006b; Jin and others, 2010; Jin and others, 2011; Brantley and others, 2011). Soils thicken from the ridge top toward the valley floor; likewise, soils in swales are thicker than on the near-planar slopes (Lin and others, 2006; Jin and Brantley, 2011). The augerable soil overlies ~1 to 2 m of coarse colluvium on the lower elevations of the south slopes (West and others, 2013; West and others, 2014). The presence of this colluvial material is consistent with observations of periglacial deposits throughout much of central Pennsylvania (Clark and Ciolkosz, 1988).

METHODS

Geologic Structure

In the SSHCZO, the bedrock does not naturally outcrop. To determine the geologic structure, eleven outcrops were investigated in four tributary drainages proximal to Shavers Creek and along the creek itself, as well as in 40 pits that were hand-dug to bedrock within SSHCZO. The strike and dip of bedding planes and

Well network at SSHCZO

Wells	Well Depth (mbls)	Completion year	Drill Type	Diameter (cm)	Casing Type	Casing Depth (mbls)	Screen
Wells #2–17	~4	2009	Power Auger	5.0	PVC	~3	Slotted Screen Bottom 1m
CZMW5–7	8	2012	Rotary Air Drill	5.0	PVC	7	Slotted Screen Bottom 1m
CZMW1–4	15	2006	Rotary Air Drill	7.6	PVC	3	Unscreened
DC1	25	2006		7.6	PVC		*Completion Error
CZMW8	30	2013		7.6	Metal/ PVC	25.43	Slotted Screen Bottom 4.57 m
DC0	50	1970		7.6	Metal	50	Open at bottom

* Completion Error indicates well was screened midway though borehole.

fractures within the Rose Hill Formation were measured in all pits and at all outcrops (fig. 1).

To assess depths of groundwater, we investigated data from 25 wells in SSHCZO ranging from 2 to 50 m in depth (fig. 1; table 1). Of these, 9 of the deepest boreholes were scanned with an optical televiewer (OTV) to characterize bedding orientation, fracture patterns, lithology and weathered zones. Three of these deep wells (CZMW5–7, numbered sequentially clockwise starting from the north along the catchment-defining ridge) were drilled to ~7.5 m deep. The southernmost deep borehole (CZMW8) was drilled to ~30 m. Five additional ~15 m deep wells are located in the valley floor: four (CZMW1–4) clustered at the outlet and one just upstream of the outlet (the "Lynch" well). A description of all wells can be found in table 1.

The OTV provides a magnetically oriented 360-degree true-color photographic image of the borehole wall as reflected in a conical mirror. The intersection of a bedding or fracture plane with the borehole creates an ellipse; unrolling the ellipse in 2D produces an oriented sine wave where the amplitude of the sine wave is the dip angle of the feature. The orientation of the images is noted so that strike and dip of fractures and bedding planes can be evaluated (Williams and Johnson, 2004).

Catchment Hydrogeochemical Condition

Groundwater flow.—Water levels were monitored monthly by hand using a Solinst water level meter in 25 wells (fig. 1; Appendix 2, table A2-1) from December 2012 to November 2013 and again in March 2014. Potentiometric surfaces were constructed from monthly groundwater level measurements using ordinary kriging in ArcGIS 9.1. Groundwater levels and temperature were monitored in CZMW1–4 from September 2013 through April 2014 using vibrating-wire pressure transducers GI-VWP-W9 (Geo-Instruments; Rhode Island) at a collection rate of every 10 minutes. Pressure transducers were corrected for barometric pressure to yield water level and temperature accuracies of $\pm$ 7 mm and $\pm$ 0.3 °C, respectively.

Groundwater age tracers.—Atmospheric tracers – tritium (^{3}H), chlorofluorocarbons (CFC-11, CFC-12, CFC-113) and sulfur hexafluoride (SF_6) – were measured to estimate the apparent groundwater ages of selected samples within the catchment (table 2). The concentrations of these constituents in the atmosphere changed since their widespread anthropogenic injection into the atmosphere starting in the 1940s (CFCs), 1950s (^{3}H), and 1970s (SF_6) (Plummer, 2005; Busenberg and Plummer, 2008),

TABLE 2

Concentration data for atmospheric tracers in SSHCZO wells. See Appendix 1 for detailed information on measurements and apparent age calculations

Well	Date	Sample Depth (mbls)	Depth to Water (mbls)	Temp (°C)	DO (mg/L)	^{3}H (TU)	error	SF$_6$ (fmol/kg)	CFC-11 (pmol/kg)	CFC-12 (pmol/kg)	CFC-113 (pmol/kg)	SF$_6$ age (years)* excess air = 0 cc L^{-1}	excess air = 2 cc L^{-1}
CZMW1	13-Apr-13	15.6	0.15	9.9	4.8	5.34	0.21	2.15	1.82	1.59	0.12	9	14
CZMW1	18-Nov-13	15.0	0.82	9.8	0.4	–	–	1.30	–	–	–	19	22
CZMW1	1-Apr-14	15.0	0.00	9.8	3.9	–	–	2.35	–	–	–	8	13
CZMW2	13-Apr-13	2.6	0.00	9.0	6.7	6.67	0.21	2.61	–	–	–	4	9
CZMW3	13-Apr-13	14.7	0.00	9.9	4.3	5.28	0.24	2.10	1.82	1.58	0.14	9	14
CZMW4	13-Apr-13	14.7	0.10	9.9	0.5	2.04	0.07	0.45	1.10	0.93	0.10	30	32
CZMW4	18-Nov-13	14.5	0.24	9.8	5.1	–	–	2.79	–	–	–	3	8
CZMW4	1-Apr-14	14.5	0.50	9.8	0.1	–	–	0.51	–	–	–	30	32
CZMW6	26-Mar-14	6.8	5.68	9.2	0.9	–	–	2.04	–	–	–	11	16
Well 2	28-Mar-14	3.5	1.12	7.1	7.6	–	–	3.09	–	–	–	1	6
Well 3	28-Mar-14	3.5	2.09	6.4	8.3	–	–	3.28	–	–	–	0	5
Well 4	28-Mar-14	3.5	1.42	6.4	4.6	–	–	1.28	–	–	–	20	23
Well 7	27-Mar-14	3.5	1.55	6.4	1.9	–	–	0.48	–	–	–	31	33
Well 8	27-Mar-14	3.5	0.82	7.5	2.2	–	–	2.63	–	–	–	5	10
Well 13	18-Nov-13	3.5	2.34	11.9	2.7	–	–	2.34	–	–	–	7	12
Well 13	26-Mar-14	3.5	2.13	7.6	6.2	–	–	2.66	–	–	–	5	10
Well 16	26-Mar-14	3.5	2.62	7.3	5.8	–	–	2.50	–	–	–	6	11

* Piston flow age (in years) using the following recharge parameters: temp = 9.8 °C and elev = 300 m.

allowing them to be used as tracers in groundwater. Each tracer is characterized by one period of time in which it best manifests the age of recharge (Davila and others, 2013), depending upon its decay rate (^{3}H half-life of 12.4 years), history of anthropogenic emission, or changes in regulatory emission standards. The tracers measured here are most useful for waters <75 years old. However, ^{3}H is the best indicator for older waters recharged between 1950 to 1970 (Plummer, 2005), CFCs for intermediate age water recharged between 1970 to 1990 (Sebol and others, 2007; Busenberg and Plummer 2008), and SF$_6$ for the youngest waters recharged between 1970 and present (Busenberg and Plummer, 2000).

All tracers were collected from wells at the outlet of the watershed (CZMW1–4) in April 2013. Following this analysis, we also surveyed groundwater more broadly for SF$_6$ analyses in November 2013 and March 2014 to estimate the variability in age for waters with residence times <10 years. In all cases, unfiltered groundwater samples were collected from shallow groundwater wells 2, 3, 4, 7, 8, 13, and 16, and deeper wells CZMW1–4 and CZMW6 (fig. 1). Concentrations of CFCs, SF$_6$, and ^{3}H were measured using standard protocols for chemical and analytical practices (Appendix 1).

Estimating apparent groundwater age — the average time period all water molecules in a given sample have resided in the saturated subsurface (Bethke and Johnson, 2008) — from these tracer concentrations is limited by accurate knowledge of the recharge conditions (for example temperature, elevation, and excess air for CFCs and SF$_6$; see Plummer and others, 2006) and groundwater flow patterns (see Bethke and Johnson, 2002). We assume average recharge conditions of 9.8 °C and an elevation of 300 m for all samples (Appendix 1). We used the Gas-Tracer-Interpretation (GTI) toolkit developed by Dávila and others (2013) to estimate the apparent ages. Of the five models employed (piston flow, exponential, exponential piston-flow, advection-dispersion, and gamma), the exponential piston-flow model fit the CZMW1-4 April 2013 well sample data the best; however, that model produced apparent groundwater ages based on SF$_6$ that were outside the possible age ranges based on assumptions of either 0 or 2 cm^3 L^{-1} of excess air (0–175 years or 2–212 years respectively). These latter estimates were also inconsistent with the ^{3}H and CFC age estimates. In contrast, the next best-fit model, the piston flow model with the assumption of 0 cm^3 L^{-1} of excess air, produced plausible ages for all samples. We therefore focus on that model.

Piston flow assumes that water moves through the system as a single closed system packet in the subsurface and thus is not exchanging or mixing with other waters along its flowpath length (Bethke and Johnson, 2002; Bethke and Johnson, 2008). Such flow is an oversimplification of groundwater flow in porous media. For example, such flow is contradictory to the observed early breakthrough and late-time tailing transport behavior of bromide in field-scale tests at SSHCZO (Kuntz and others, 2011). The error introduced by using the piston flow model here will result in a young bias to our interpretation; however, the pattern in apparent ages (young, intermediate and old) is a robust inference because it does not depend on the modeled flow assumption.

Solute sampling and analysis.—To determine the geochemistry of groundwater, samples were also collected monthly to bimonthly at Shale Hills from December 2012 through March 2014 for chemical analysis (table 3). Groundwater samples were collected at 25 wells when water was present, while surface water samples were collected from the stream near the weir at the outlet of the watershed for each sampling event. When possible, stream waters were also collected adjacent to Well 8 and Well 11 (fig. 1). All water samples were collected using a peristaltic pump and filtered inline using EPA-approved 0.45 µm groundwater sampling capsules (Polyether-sulfone filter; Millipore Inc.). For a given sampling event, three samples were collected at each sampling location and analyzed for alkalinity, major anions, and cations. The

TABLE 3

Average and standard error of chemical constituents analyzed in the groundwater and stream water, where n represents the number of samples taken at each location from 2013-2014

Site	Water Type	Well depth (m)	n	Alkalinity (μmol L⁻¹)	Cl⁻ (μmol L⁻¹)	SO₄²⁻ (μmol L⁻¹)	NO₃⁻ (μmol L⁻¹)	Al³⁺ (μmol L⁻¹)	Ca²⁺ (μmol L⁻¹)	Fe³⁺ (μmol L⁻¹)	K⁺ (μmol L⁻¹)	Mg²⁺ (μmol L⁻¹)	Mn³⁺ (μmol L⁻¹)	Na⁺ (μmol L⁻¹)	Si (μmol L⁻¹)	Sr²⁺ (μmol L⁻¹)
Well 2	GW	<4	11	2414 ± 303	40.7 ± 1.7	139 ± 4.2	2.6 ± 1.5	5.42 ± 2.41	1375 ± 51	2.61 ± 1.45	14.5 ± 0.6	140 ± 9.3	1.1 ± 0.8	31 ± 1.6	108 ± 2.3	0.79 ± 0.02
Well 3	GW	<4	11	1663 ± 175	37.8 ± 5.5	128 ± 7.1	2.2 ± 0.6	4.66 ± 1.31	1070 ± 40	2.20 ± 0.63	13.0 ± 0.7	121 ± 9.2	2.3 ± 1.6	59 ± 18.2	111 ± 2.2	0.82 ± 0.04
Well 4	GW	<4	11	988 ± 125	29.7 ± 7.3	124 ± 6.1	2.2 ± 0.7	6.02 ± 1.70	389 ± 22	2.16 ± 0.65	21.6 ± 1.5	253 ± 12.4	2.9 ± 1.8	69 ± 10.1	113 ± 3.7	1.09 ± 0.06
Well 5	GW	<4	11	729 ± 163	23.5 ± 2.7	94 ± 6.3	1.4 ± 0.9	2.44 ± 1.01	357 ± 76	1.38 ± 0.94	27.0 ± 1.2	146 ± 25.4	1.1 ± 0.8	26 ± 5.0	107 ± 2.9	0.26 ± 0.05
Well 6	GW	<4	11	1460 ± 179	19.7 ± 1.3	126 ± 8.0	1.1 ± 1.1	1.97 ± 0.60	567 ± 43	1.12 ± 1.12	24.6 ± 0.9	346 ± 31.3	0.9 ± 0.9	186 ± 20.6	114 ± 1.7	1.16 ± 0.13
Well 7	GW	<4	11	1294 ± 136	30.5 ± 5.0	180 ± 6.9	0.9 ± 0.3	3.68 ± 0.93	529 ± 18	0.94 ± 0.33	21.5 ± 0.5	450 ± 24.2	5.0 ± 2.0	131 ± 3.3	152 ± 4.9	2.89 ± 0.23
Well 8	GW	<4	11	490 ± 79	32.6 ± 7.7	104 ± 6.3	14.8 ± 3.5	4.97 ± 1.30	162 ± 22	14.76 ± 3.50	36.0 ± 2.5	171 ± 22.2	13.0 ± 2.6	58 ± 14.2	114 ± 1.7	0.27 ± 0.02
Well 9	GW	<4	7	289 ± 74	31.9 ± 9.0	123 ± 3.8	1.7 ± 0.6	4.55 ± 1.77	103 ± 12	1.67 ± 0.58	21.0 ± 1.1	108 ± 11.0	1.6 ± 1.3	55 ± 16.3	122 ± 6.2	0.08 ± 0.01
Well 10	GW	<4	11	200 ± 35	22.9 ± 1.6	116 ± 3.8	4.0 ± 2.5	5.17 ± 0.99	95 ± 10	3.95 ± 2.52	30.4 ± 0.5	101 ± 7.4	5.4 ± 2.6	31 ± 2.9	116 ± 2.5	0.17 ± 0.02
Well 11	GW	<4	11	229 ± 34	22.8 ± 1.8	86 ± 5.4	0.9 ± 0.5	2.01 ± 0.40	93 ± 6	0.94 ± 0.47	24.1 ± 0.5	109 ± 7.8	0.7 ± 0.7	34 ± 1.2	122 ± 2.6	0.13 ± 0.01
Well 12	GW	<4	6	214 ± 68	22.7 ± 2.2	88 ± 4.0	11.7 ± 4.3	11.80 ± 4.38	71 ± 11	11.69 ± 4.32	24.1 ± 0.7	67 ± 4.5	3.6 ± 1.8	49 ± 6.2	113 ± 4.9	0.10 ± 0.01
Well 13	GW	<4	11	1325 ± 175	30.2 ± 6.7	158 ± 5.3	7.2 ± 2.9	9.27 ± 3.53	487 ± 50	7.18 ± 2.91	31.3 ± 1.6	504 ± 47.5	3.2 ± 1.8	92 ± 13.9	115 ± 4.3	0.40 ± 0.03
Well 14	GW	<4	10	546 ± 74	20.8 ± 1.3	124 ± 9.2	4.9 ± 2.1	2.87 ± 0.82	216 ± 23	4.91 ± 2.12	43.7 ± 1.4	264 ± 27.5	7.2 ± 2.0	39 ± 3.3	143 ± 5.9	0.17 ± 0.02
Well 15	GW	<4	5	1039 ± 131	37.7 ± 10.7	101 ± 15.1	8.5 ± 2.8	9.59 ± 2.18	311 ± 125	8.47 ± 2.78	43.3 ± 5.0	183 ± 31.5	12.0 ± 2.5	23 ± 4.4	162 ± 18.9	0.39 ± 0.11
Well 16	GW	<4	9	513 ± 57	25.3 ± 1.5	85 ± 7.5	12.1 ± 2.9	2.53 ± 1.81	176 ± 11	12.05 ± 2.86	28.2 ± 0.6	258 ± 6.3	6.0 ± 2.0	61 ± 1.7	121 ± 5.8	0.19 ± 0.02
Well 17	GW	<4	11	1938 ± 199	52.4 ± 2.7	118 ± 2.8	6.4 ± 4.9	4.38 ± 2.45	1164 ± 34	6.41 ± 4.87	13.3 ± 0.7	218 ± 11.6	1.2 ± 1.0	42 ± 2.0	106 ± 2.5	0.91 ± 0.02
CZMW1	GW	15	11	2311 ± 238	28.5 ± 1.0	172 ± 36.1	4.8 ± 1.0	4.52 ± 2.36	1158 ± 45	7.23 ± 4.25	24.5 ± 1.1	388 ± 16.4	9.8 ± 3.5	117 ± 30.1	116 ± 4.0	3.29 ± 0.45
CZMW2	GW	9	9	2009 ± 166	31.1 ± 1.1	148 ± 32.9	3.0 ± 1.2	4.77 ± 1.56	1359 ± 19	2.76 ± 1.42	15.9 ± 0.4	192 ± 24.7	1.5 ± 1.4	30 ± 2.9	111 ± 1.5	1.34 ± 0.15
CZMW3	GW	15	9	2002 ± 137	31.6 ± 0.9	162 ± 35.5	2.6 ± 1.1	6.53 ± 2.11	1253 ± 18	2.50 ± 0.66	20.8 ± 0.5	323 ± 13.1	1.3 ± 1.1	39 ± 3.6	110 ± 2.4	1.94 ± 0.14
CZMW4	GW	14.5	9	2064 ± 128	30.2 ± 1.4	165 ± 32.2	3.8 ± 0.9	6.45 ± 3.55	1184 ± 69	5.65 ± 2.13	21.9 ± 0.9	327 ± 39.1	5.5 ± 2.6	160 ± 52.9	122 ± 4.2	4.33 ± 0.88
CZMW5	GW	<8	7	2303 ± 241	48.7 ± 3.5	119 ± 15.0	14.0 ± 9.3	3.57 ± 2.34	870 ± 24	56.05 ± 13.14	104.8 ± 1.2	642 ± 45.8	26.2 ± 3.2	60 ± 3.4	234 ± 15.0	1.34 ± 0.04
CZMW6	GW	<8	11	2737 ± 355	37.7 ± 7.0	62 ± 7.8	116.5 ± 106.4	3.51 ± 1.57	770 ± 33	129.07 ± 25.73	90.2 ± 1.6	853 ± 48.3	158.1 ± 7.3	79 ± 5.2	132 ± 6.5	1.03 ± 0.07
CZMW7	GW	<8	9	2998 ± 371	52.4 ± 16.4	109 ± 22.8	11.5 ± 3.8	5.04 ± 3.43	1309 ± 103	17.10 ± 10.44	57.9 ± 2.2	744 ± 62.8	28.6 ± 5.1	284 ± 24.7	93 ± 7.9	1.44 ± 0.14
CZMW8D	GW	30.1	9	1003 ± 135	87.5 ± 49.5	182 ± 38.7	6.5 ± 2.4	7.13 ± 3.36	364 ± 22	4.36 ± 3.50	25.2 ± 1.9	482 ± 11.0	5.4 ± 1.7	224 ± 29.0	172 ± 18.3	0.53 ± 0.07
DC0	GW	50	9	734 ± 123	95.8 ± 8.2	8 ± 2.2	3.4 ± 1.2	<0.005	313 ± 7	23.57 ± 23.57	70.2 ± 2.1	260 ± 5.4	1.2 ± 0.6	123 ± 19.7	13 ± 1.0	0.53 ± 0.01
SW11	SW	--	3	253 ± 10	39.5 ± 21.2	88 ± 2.4	9.1 ± 0.6	1.90 ± 0.65	75 ± 14	<0.005	19.1 ± 2.7	96 ± 16.9	<0.005	58 ± 39.3	90 ± 2.1	0.08 ± 0.01
SW8	SW	--	5	396 ± 200	36.5 ± 13.4	84 ± 5.3	6.9 ± 2.0	2.13 ± 0.46	186 ± 119	1.52 ± 1.52	30.8 ± 3.3	109 ± 22.1	<0.005	40 ± 16.6	100 ± 6.0	0.20 ± 0.12
Wier	SW	--	8	599 ± 15	22.9 ± 3.1	102 ± 6.8	4.7 ± 1.2	1.13 ± 0.39	265 ± 89	1.52 ± 1.52	28.8 ± 3.0	111 ± 18.6	7.9 ± 3.3	48 ± 1.6	85 ± 11.4	0.32 ± 0.06

Table 4

The minimum, average and maximum groundwater calcite saturation state

Well	Min	Average	Max
2	-1.53	-0.75	0.07
3	-1.74	-1.24	-0.53
4	-2.66	-1.74	-0.99
5	-3.45	-2.54	-0.95
6	-2.17	-1.18	-0.32
7	-2.59	-1.34	-0.69
8	-3.82	-2.83	-1.29
9	-4.16	-3.57	-2.27
10	-4.54	-3.79	-2.40
11	-4.39	-3.67	-2.60
12	-4.43	-3.67	-2.98
13	-2.37	-1.75	-1.24
14	-3.53	-2.81	-2.04
15	-2.21	-2.06	-1.83
16	-3.32	-2.90	-2.51
17	-1.42	-0.86	-0.09
CZMW1	-0.62	-0.13	0.40
CZMW2	-0.85	-0.56	-0.32
CZMW3	-0.69	-0.51	-0.28
CZMW4	-0.66	-0.42	-0.22
CZMW5	-1.50	-1.22	-0.81
CZMW6	-1.91	-1.41	-0.96
CZMW7	-1.13	-0.57	-0.20
CZMW8	-1.71	-0.78	-0.27
CZMW8D	-2.08	-1.40	-0.69
DC0	-1.96	-1.42	-0.65

All groundwater was sampled from the bottom of the wells.

latter were measured on 60 mL samples that were acidified with 3 drops of pure nitric acid in the laboratory after filtration in the field. Field parameters (pH, specific conductivity (μScm^{-1}) and temperature) were measured at all locations using either a YSI Professional Plus^{TM} multiprobe or a VWR SP70 Symphony pH probe and Mettler Toledo conductivity probe. Because CZMW1–4 are unscreened boreholes (table 1), field parameters [pH, conductivity, temperature, and dissolved oxygen (DO)] were also profiled at 1-m depth intervals downhole, using the YSI multiprobe.

Anions were measured on a Dionex Ion Chromatograph (ICS-250; Sunnyvale, California), while major cations and dissolved silica were analyzed on an inductively coupled plasma-optical emission spectrometer (ICP-OES PS300UV, Teledyne Leeman Labs, Hudson, NH). The analytical precision for major ion analysis was ~3 percent on the major elements and ~10 percent for minor elements. Total alkalinity was calculated as HCO_3^- (meq L^{-1}) and determined by end-point titration (pH of 3) with 0.1 N HCl using a digital burette within 48 h of collection.

The saturation index, SI, was calculated using PHREEQC for calcite (Parkhurst and Appelo, 1999; table 4). Field (temperature, conductivity and pH) and laboratory measurements (alkalinity and ion concentrations) were used as the inputs. Negative SI

values denote groundwaters undersaturated with respect to a given mineral, indicating the potential for mineral dissolution. Positive values are indicative of supersaturated conditions, or the potential for mineral precipitation. SI values of 0.00 ± 0.05 were interpreted to represent chemical equilibrium. To evaluate the spatial variability in the groundwater chemistry and mineral saturation index (SI), the average annual SI value and major cation concentrations (μmol L^{-1}) were spatially interpolated and contoured using ordinary kriging (ArcGIS 9.1).

Regolith Weathering and Mineralogical Analysis

Regolith geochemistry.—Bulk drill core samples from CZMW 5 to 8 were chemically analyzed (tables 5, 6, 7 and 8) to investigate weathering. Samples were then compared to previously reported analyses of drilled material from wells CZMW 1 to 4 on the valley floor (Kuntz and others, 2011; Brantley and others, 2013) and DC1 at the ridge top (see table 1 for well details; Jin and others, 2010; Brantley and others, 2013). After drying, each bulk sample was ground to particles <150 μm (100-mesh sieve). Samples were then fused with Li metaborate, and dissolved using standard methods (Feldman, 1983), and then analyzed using inductively coupled plasma atomic emission spectroscopy (ICP-AES; precision of $\pm3\%$) following previous work (Brantley and others, 2013). Loss on ignition (LOI) was measured from ashing samples to 900 °C for the metaborate fusion.

Samples from CZWM 5 to 8 were also analyzed for total sulfur (table 9), while samples from CZMW 7 to 8 were additionally analyzed for ferrous iron (Fe^{2+}; table 9). Total sulfur was measured using potassium iodate (KIO_3) titration on a LECO Sulfur Coulometer (Jones and Isaac, 1972). Accuracy and precision were determined by analyzing one calibration standard (0.0288% sulfur; LECO) repeatedly, one low-sulfur standard (0.0025% sulfur; LGW1 85-quartz diorite sample previously analyzed by LECO, Inc.) and four unknown samples measured six times each. Ferrous iron concentrations (FeO wt%) were determined through titration (Goldich, 1984). The USGS Cody Shale SCO-1 (0.90% FeO) with a low organic content was used as a reference material. This method only quantifies the ferrous iron associated with silicate minerals and iron oxides.

Carbon content and isotopic ratios were also examined on samples from the ridgetop drilled material (table 10) to map the presence of trace carbonate minerals (ankerite and calcite; Jin and others 2010). Total carbon content and isotopic data were measured using a Costech Elemental Analyzer and Thermo Gas Bench, respectively, with a low carbon check standard.

Mass transfer coefficients, τ_{ij}, were calculated to investigate the change in soil/ rock elemental concentrations, C, with depth, through comparison of the weight percent (on the received basis) soluble element, j, to that of an insoluble element, i, (such as Zr or Ti) in weathered material (subscript w), compared to that of the parent material (subscript p), as described by the following equation (Brimhall and Dietrich; 1987; Anderson and others, 2002):

$$\tau_{i,j} = \frac{C_{j,w}C_{i,p}}{C_{j,p}C_{i,w}} - 1$$

The material is enriched compared to the insoluble element in the parent material when τ_{ij} is positive and depleted when τ_{ij} is negative. Zr was chosen as the immobile element because it is present in the least soluble of the observed minerals, zircon (Jin and others, 2010). The choice of parent composition is discussed further below.

Calculations of $\tau_{Zr,j}$ yield estimates of depletion or addition of elements with respect to Zr assuming that the Zr in parent composition is uniform. Traditionally, such mobilization is attributed to solubilization and transport of species as solutes. This

Table 5

Elemental concentrations and τ values from CZMW5 (borehole DC6)

		Elemental Concentrations											τ_{Zri}									
Sample ID	Depth (mbls)	Al(%)	Ca(%)	Fe(%)	K(%)	Mg(%)	Mn(%)	Na(%)	P(%)	Si(%)	Ti(%)	Zr (ppm)	Al	Ca	Fe	K	Mg	Mn	Na	P	Si	Ti
DC6-0-1	0.31	10.5	0.13	5.04	3.76	0.81	0.04	0.27	0.05	26.8	0.58	160	-0.05	-0.31	-0.14	-0.06	-0.38	-0.08	-0.14	0.17	-0.05	-0.05
DC6-1-2	0.61	10.7	0.14	5.43	3.87	0.85	0.07	0.27	0.04	26.2	0.59	189	-0.18	-0.37	-0.22	-0.18	-0.45	0.36	-0.27	-0.20	-0.21	-0.18
DC6-2-3	0.91	11.1	0.14	5.27	4.00	0.85	0.05	0.28	0.03	27.3	0.59	177	-0.10	-0.33	-0.19	-0.10	-0.41	0.03	-0.19	-0.37	-0.12	-0.13
DC6-3-4	1.22	11.3	0.13	5.21	3.85	0.81	0.06	0.26	0.04	26.9	0.60	178	-0.08	-0.38	-0.20	-0.13	-0.44	0.23	-0.25	-0.16	-0.14	-0.12
DC6-4-5	1.52	11.7	0.12	5.18	3.84	0.76	0.07	0.25	0.05	26.5	0.58	161	-0.01	-0.37	-0.12	-0.04	-0.42	0.59	-0.21	0.16	-0.06	-0.06
DC6-5-6	1.83	11.2	0.13	5.19	3.79	0.77	0.04	0.26	0.05	26.7	0.57	170	-0.05	-0.35	-0.17	-0.11	-0.45	-0.14	-0.22	0.10	-0.11	-0.13
DC6-6-7	2.13	10.5	0.12	5.30	3.66	0.73	0.04	0.27	0.05	27.7	0.57	205	-0.26	-0.50	-0.29	-0.28	-0.56	-0.28	-0.33	-0.08	-0.23	-0.27
DC6-7-8	2.44	10.4	0.11	5.03	3.75	0.73	0.03	0.28	0.05	26.9	0.58	203	-0.26	-0.54	-0.33	-0.26	-0.56	-0.46	-0.30	-0.08	-0.25	-0.25
DC6-10-11	3.35	10.5	0.11	5.30	3.79	0.79	0.02	0.27	0.04	26.9	0.58	180	-0.16	-0.48	-0.20	-0.16	-0.46	-0.59	-0.23	-0.17	-0.15	-0.16
DC6-11-12	3.96	10.6	0.10	5.69	3.75	0.76	0.08	0.27	0.05	26.5	0.56	152	0.01	-0.44	0.02	-0.01	-0.39	0.93	-0.09	0.23	-0.01	-0.04
DC6-14-15	4.57	11.4	0.11	5.36	3.83	0.82	0.03	0.25	0.06	27.0	0.58	155	0.06	-0.40	-0.06	-0.01	-0.35	-0.29	-0.18	0.45	-0.01	-0.02
DC6-17-18	5.48	10.3	0.10	5.30	3.57	0.76	0.14	0.25	0.04	27.2	0.54	204	-0.27	-0.59	-0.29	-0.30	-0.54	1.51	-0.37	-0.27	-0.24	-0.31
DC6-20-21	6.40	10.0	0.11	5.11	3.64	0.85	0.03	0.26	0.05	27.6	0.55	184	-0.21	-0.49	-0.24	-0.21	-0.43	-0.40	-0.28	0.02	-0.15	-0.22
DC6-22-23	7.01	10.6	0.10	5.43	3.80	0.85	0.07	0.26	0.03	26.9	0.56	158	-0.04	-0.47	-0.06	-0.04	-0.34	0.62	-0.16	-0.29	-0.03	-0.08
DC6-23-24	7.31	11.4	0.10	5.59	3.95	0.87	0.03	0.27	0.05	26.0	0.58	179	-0.08	-0.53	-0.15	-0.12	-0.40	-0.39	-0.23	0.05	-0.17	-0.15
DC6-24-25	7.62	10.8	0.10	5.35	3.92	0.86	0.04	0.28	0.04	26.7	0.58	181	-0.14	-0.53	-0.20	-0.14	-0.42	-0.19	-0.21	-0.17	-0.16	-0.17

Values determined on a received basis.

TABLE 6

Elemental concentrations and τ values from CZMW6 (borehole DC7)

		Elemental Concentrations											τ_{Zr}									
SampleID	Depth(mbls)	Al(%)	Ca(%)	Fe(%)	K(%)	Mg(%)	Mn(%)	Na(%)	P(%)	Si(%)	Ti(%)	Zr(ppm)	Al	Ca	Fe	K	Mg	Mn	Na	P	Si	Ti
DC7-0-1	0.31	10.9	0.05	5.66	3.92	0.84	0.05	0.26	0.05	26.9	0.55	174	-0.09	-0.76	-0.11	-0.10	-0.41	0.05	-0.24	0.08	-0.12	-0.17
DC7-1-2	0.61	10.6	0.05	5.66	3.67	0.83	0.11	0.22	0.07	26.7	0.53	176	-0.13	-0.76	-0.12	-0.17	-0.42	1.29	-0.36	0.49	-0.14	-0.21
DC7-2-3	0.91	10.5	0.08	5.76	3.82	0.90	0.06	0.24	0.04	26.7	0.54	169	-0.10	-0.60	-0.07	-0.10	-0.35	0.30	-0.27	-0.11	-0.10	-0.17
DC7-3-4	1.22	11.9	0.06	5.66	4.23	0.92	0.03	0.24	0.05	26.6	0.57	159	0.08	-0.68	-0.03	0.06	-0.29	-0.31	-0.23	0.18	-0.05	-0.06
DC7-4-5	1.52	11.4	0.06	5.50	4.01	0.86	0.04	0.24	0.05	27.4	0.58	192	-0.14	-0.74	-0.22	-0.16	-0.45	-0.24	-0.36	-0.02	-0.19	-0.21
DC7-5-6	1.83	10.2	0.09	5.80	3.65	0.87	0.14	0.22	0.05	28.8	0.53	249	-0.41	-0.69	-0.37	-0.41	-0.57	1.06	-0.55	-0.25	-0.34	-0.44
DC7-6-7	2.13	11.5	0.09	5.47	4.13	0.95	0.03	0.24	0.06	27.0	0.58	175	-0.05	-0.57	-0.15	-0.06	-0.34	-0.37	-0.30	0.29	-0.12	-0.13
DC7-7-8	2.44	11.5	0.08	6.26	4.14	0.95	0.07	0.23	0.06	25.7	0.55	168	-0.01	-0.60	0.02	-0.01	-0.31	0.53	-0.30	0.34	-0.13	-0.14
DC7-9-10	3.05	11.8	0.08	5.94	4.22	0.94	0.04	0.24	0.05	26.1	0.58	152	0.12	-0.56	0.06	0.11	-0.24	-0.04	-0.19	0.23	-0.02	0.00
DC7-10-11	3.35	11.1	0.09	5.26	4.02	0.94	0.03	0.24	0.04	27.1	0.59	174	-0.08	-0.56	-0.18	-0.08	-0.34	-0.37	-0.30	-0.14	-0.11	-0.11
DC7-11-12	3.96	10.8	0.08	5.64	3.99	0.94	0.04	0.25	0.05	26.3	0.59	161	-0.03	-0.58	-0.05	-0.01	-0.29	-0.09	-0.21	0.16	-0.07	-0.04
DC7-14-15	4.57	11.24	0.08	5.86	4.08	0.93	0.09	0.25	0.04	26.7	0.57	168	-0.03	-0.60	-0.05	-0.03	-0.32	0.96	-0.24	-0.11	-0.10	-0.11
DC7-15-16	4.87	10.69	0.08	5.42	3.94	0.97	0.06	0.25	0.04	26.7	0.56	178	-0.13	-0.62	-0.17	-0.11	-0.33	0.23	-0.28	-0.16	-0.15	-0.18
DC7-17-18	5.49	10.71	0.08	5.76	3.97	0.97	0.06	0.24	0.04	26.8	0.55	180	-0.14	-0.62	-0.13	-0.12	-0.34	0.22	-0.32	-0.17	-0.15	-0.20
DC7-20-21	6.40	10.91	0.06	5.32	4.24	0.99	0.02	0.25	0.03	26.8	0.59	168	-0.06	-0.70	-0.14	0.01	-0.28	-0.56	-0.24	-0.33	-0.09	-0.08
DC7-22-23	7.01	11.14	0.08	5.48	4.33	1.08	0.02	0.26	0.04	26.3	0.61	162	-0.01	-0.58	-0.08	0.07	-0.18	-0.55	-0.18	-0.07	-0.08	-0.02
DC7-23-24	7.32	11.00	0.09	5.75	4.31	1.11	0.04	0.27	0.03	26.8	0.58	162	-0.02	-0.53	-0.03	0.06	-0.16	-0.10	-0.15	-0.31	-0.06	-0.06
DC7-24-25	7.62	11.30	0.09	5.84	4.29	1.12	0.03	0.26	0.03	25.7	0.60	154	0.06	-0.51	0.03	0.11	-0.11	-0.29	-0.14	-0.27	-0.05	0.02

Values determined on a received basis.

TABLE 7

Elemental concentrations and τ values from CZMW7 (borehole DC8)

Sample ID	Depth (mbls)	Elemental Concentrations											$\tau_{Zr,i}$									
		Al (%)	Ca (%)	Fe (%)	K (%)	Mg (%)	Mn (%)	Na (%)	P (%)	Si (%)	Ti (%)	Zr (ppm)	Al	Ca	Fe	K	Mg	Mn	Na	P	Si	Ti
DC8-0-1	0.31	10.5	0.02	5.40	3.61	0.71	0.05	0.23	0.08	27.8	0.62	260	-0.42	-0.93	-0.43	-0.44	-0.67	-0.30	-0.55	0.15	-0.39	-0.38
DC8-1-2	0.61	10.5	0.02	5.03	3.72	0.74	0.02	0.24	0.05	27.2	0.60	200	-0.24	-0.92	-0.31	-0.26	-0.55	-0.63	-0.39	-0.06	-0.23	-0.22
DC8-2-3	0.91	10.4	0.03	6.12	3.60	0.77	0.06	0.21	0.07	26.8	0.59	226	-0.34	-0.89	-0.26	-0.36	-0.58	-0.03	-0.53	0.16	-0.32	-0.32
DC8-3-4	1.22	11.2	0.02	5.90	3.88	0.79	0.03	0.23	0.06	25.9	0.61	179	-0.10	-0.91	-0.10	-0.13	-0.46	-0.39	-0.34	0.26	-0.18	-0.11
DC8-4-5	1.52	10.7	0.03	5.90	3.72	0.81	0.05	0.23	0.05	28.0	0.61	193	-0.20	-0.87	-0.17	-0.23	-0.49	-0.05	-0.39	-0.03	-0.17	-0.17
DC8-5-6	1.83	10.6	0.07	5.53	3.81	0.83	0.04	0.23	0.05	27.0	0.60	185	-0.17	-0.68	-0.19	-0.18	-0.45	-0.21	-0.36	0.01	-0.19	-0.15
DC8-6-7	2.13	10.5	0.06	5.82	3.74	0.85	0.04	0.22	0.05	28.1	0.59	198	-0.24	-0.74	-0.20	-0.24	-0.47	-0.26	-0.43	-0.05	-0.19	-0.22
DC8-7-8	2.44	10.4	0.07	5.74	3.74	0.85	0.08	0.23	0.05	27.5	0.61	190	-0.21	-0.69	-0.18	-0.21	-0.45	0.54	-0.38	-0.01	-0.18	-0.16
DC8-10-11	3.35	8.4	0.06	5.26	2.82	0.72	0.08	0.23	0.04	31.2	0.59	334	-0.64	-0.85	-0.57	-0.66	-0.74	-0.12	-0.65	-0.55	-0.47	-0.54
DC8-12-13	3.96	10.8	0.09	5.26	4.03	0.93	0.04	0.23	0.05	27.0	0.57	191	-0.18	-0.60	-0.25	-0.16	-0.40	-0.23	-0.38	-0.02	-0.20	-0.22
DC8-14-15	4.57	10.3	0.08	5.64	3.81	0.92	0.04	0.24	0.04	27.3	0.56	182	-0.19	-0.63	-0.16	-0.16	-0.38	-0.20	-0.33	-0.18	-0.15	-0.20
DC8-17-18	5.48	11.5	0.08	5.50	4.37	0.95	0.02	0.27	0.04	26.3	0.61	157	0.06	-0.57	-0.05	0.11	-0.26	-0.53	-0.12	-0.05	-0.05	0.01
DC8-20-21	6.40	10.1	0.09	7.07	3.55	0.88	0.19	0.22	0.10	27.6	0.54	222	-0.34	-0.66	-0.13	-0.36	-0.51	2.13	-0.49	0.69	-0.29	-0.36
DC8-22-23	7.01	10.7	0.11	5.88	3.86	0.89	0.07	0.22	0.07	26.6	0.59	185	-0.16	-0.50	-0.13	-0.16	-0.41	0.39	-0.39	0.42	-0.18	-0.17
DC8-23-24	7.31	10.1	0.08	5.13	3.55	0.84	0.05	0.22	0.05	28.3	0.56	219	-0.34	-0.69	-0.36	-0.35	-0.53	-0.16	-0.49	-0.14	-0.26	-0.33
DC8-24-25	7.62	11.0	0.10	5.17	3.95	0.91	0.03	0.23	0.05	27.8	0.60	190	-0.16	-0.56	-0.26	-0.17	-0.41	-0.42	-0.38	-0.01	-0.17	-0.18

Values determined on a received basis.

TABLE 8

Elemental concentrations and τ values from CZMW8 (borehole DC9)

Sample ID	Depth (mbls)	Al (%)	Ca (%)	Fe (%)	K (%)	Mg (%)	Mn (%)	Na (%)	P (%)	Si (%)	Ti (%)	Zr (ppm)	LOI (%)	τ_Zr Al	Ca	Fe	K	Mg	Mn	Na	P	Si	Ti
						Elemental Concentrations																	
DC9-0-1.75	0.27	10.1	0.12	5.01	3.61	0.87	0.08	0.20	0.05	28.5	0.62	187	7.37	-0.22	-0.46	-0.27	-0.23	-0.43	0.65	-0.44	-0.02	-0.13	-0.14
DC9-1.75-4.5	0.88	10.3	0.07	5.08	3.82	0.87	0.05	0.19	0.03	27.7	0.59	159	6.56	-0.06	-0.62	-0.13	-0.04	-0.33	0.22	-0.38	-0.28	-0.01	-0.03
DC9-19-20	5.94	11.2	0.09	5.25	4.24	1.06	0.02	0.23	0.04	28.0	0.62	163	6.42	-0.01	-0.54	-0.13	0.04	-0.21	-0.66	-0.28	0.02	-0.03	-0.01
DC9-30.1	9.17	11.2	0.05	5.31	4.24	1.14	0.01	0.25	0.04	27.9	0.62	147	6.23	0.10	-0.70	-0.02	0.15	-0.05	-0.66	-0.14	-0.11	0.08	0.10
DC9-39-40	12.04	10.8	0.09	5.57	3.94	1.15	0.10	0.22	0.07	27.1	0.59	153	6.27	0.02	-0.52	-0.01	0.03	-0.08	1.46	-0.26	0.63	0.01	0.01
DC9-50.4	15.36	10.5	0.11	5.22	4.04	1.22	0.02	0.25	0.06	28.2	0.59	141	5.86	0.08	-0.35	0.01	0.14	0.06	-0.36	-0.09	0.50	0.14	0.09
DC9-51.0	15.27	10.7	0.06	5.30	3.95	1.18	0.02	0.25	0.03	28.3	0.60	152	5.93	0.02	-0.67	-0.05	0.04	-0.05	-0.55	-0.15	-0.24	0.05	0.03
DC9-51.9	15.82	11.4	0.14	5.56	4.35	1.29	0.04	0.23	0.08	26.8	0.58	132	6.24	0.24	-0.10	0.15	0.32	0.19	0.05	-0.11	1.19	0.15	0.14
DC9-52.1	15.88	9.3	0.08	5.18	3.13	1.24	0.02	0.31	0.05	30.6	0.57	209	4.45	-0.36	-0.69	-0.32	-0.40	-0.27	-0.66	-0.24	-0.17	-0.17	-0.29
DC9-52.5	16.00	10.7	0.06	5.24	3.99	1.25	0.02	0.28	0.03	27.7	0.60	149	5.25	0.03	-0.63	-0.04	0.07	0.02	-0.43	-0.05	-0.24	0.06	0.05
DC9-53.8	16.40	11.6	0.06	5.15	4.47	1.36	0.02	0.28	0.04	27.1	0.63	145	5.28	0.16	-0.63	-0.03	0.23	0.14	-0.50	0.00	0.03	0.09	0.13
DC9-61-62	18.75	10.4	0.13	5.08	3.90	1.26	0.03	0.28	0.04	27.1	0.58	149	5.09	0.01	-0.25	-0.07	0.05	0.03	-0.25	-0.04	-0.06	0.03	0.02
DC9-70-71	21.49	11.0	0.10	5.13	4.26	1.25	0.02	0.23	0.05	27.4	0.61	143	5.42	0.11	-0.39	-0.02	0.19	0.07	-0.36	-0.17	0.24	0.09	0.12
DC9-85.2-83	25.63	9.9	0.11	7.18	3.24	1.37	0.05	0.18	0.03	26.8	0.54	142	5.99	0.01	-0.37	0.38	-0.09	0.18	0.20	-0.34	-0.17	0.07	-0.01
DC9-95.0	28.96	10.6	0.11	5.18	3.94	1.31	0.03	0.32	0.03	29.1	0.63	167	4.88	-0.08	-0.45	-0.15	-0.05	-0.04	-0.40	-0.01	-0.36	-0.01	-0.02
DC9-100-101	30.63	11.4	0.16	5.70	4.29	1.39	0.03	0.27	0.05	27.4	0.61	138	5.19	0.19	-0.01	0.12	0.24	0.23	-0.23	-0.02	0.28	0.13	0.16
Average Parent		10.7	0.18	5.67	3.86	1.26	0.04	0.30	0.04	27.2	0.59	155											

Values determined on a received basis.

Sulfur (S) and ferrous iron (FeO) concentrations (wt%) in CZMW8 (borehole DC9)

Sample ID	Depth (mbls)	S (wt%)	FeO (wt%)
DC9-0-1.75	0.27	0.006	1.40
DC9-1.75-4.5	0.88	0.007	ND
DC9-19-20	5.94	0.001	1.86
DC9-39-40	12.04	0.005	ND
DC9-50.4	15.36	0.002	2.75
DC9-51.0	15.27	0.055	ND
DC9-51.9	15.82	0.011	ND
DC9-52.1	15.88	0.094	4.79
DC9-53.8	16.40	0.142	ND
DC9-61-62	18.75	0.122	4.51
DC9-100-101	30.63	0.113	4.37

Values are presented on received basis. ND indicates that analysis were not determined on the samples.

solubilization preferentially removes some elements relative to others, allowing this transport mechanism to be distinguished from physical erosion, which generally is considered to remove all material homogeneously from the system (Jin and others, 2010). However, much of the depletion of Al, Ca, Fe, K, Mg, Na, and Si observed in soils in Shale Hills has been attributed to mobilization of very fine clay particles that leave zircons behind (Jin and others, 2010; Yesavage and others, 2012; Noireaux and others, 2014; Sullivan and others, 2016). This phenomenon is not unique to SSHCZO. For example, Bern and others (2011, 2015) demonstrated clay and colloid transport contributes significantly to downslope mass transfer when compared with the dissolved load along a granitic catena (Kruger National Park, South Africa). Here, we assessed transport as a solute versus particle+solute by setting either Al or Zr as the insoluble element in τ calculations. Specifically, elements depleted compared to Zr were assumed to have been transported either as solutes or fine particles (leaving zircons behind) but elements depleted compared to Al were assumed to have been transported strictly as solutes. The differences between these two estimates yield an assessment of elements mobilized as fine Al-containing clay particles.

Carbon isotopes ($\delta^{13}C$) for CZMW8 (borehole DC9)

Borehole	Depth (m)	$\delta^{13}C$ (VPDB)	C (%)
DC9-0-1.75	0.27	-30.2	0.53
DC9-19-20	5.94	-26.5	0.06
DC9-39-40	12.04	-24.2	0.05
DC9-50.4	15.36	-22.4	0.03
DC9-51.0	15.27	-25.8	0.08
DC9-61-62	18.75	-21.5	0.08
DC9-100-101	30.63	-22.9	0.12
DC8-7-8	2.29	-24.5	0.10
DC8-24-25	7.47	-25.6	0.07

In using the mass transfer coefficient τ to assess element loss or gain, the most difficult consideration is choice of parent composition. This is especially true in a sedimentary rock with stratigraphic variations. Sometimes, an average value is used for the entire catchment whereas in other studies, the bottom samples from a given profile are used to estimate the parent. In previous publications about this catchment, we assessed parent either as a composite average from borehole DC1 of samples from 0.3 to 20 m (that is saprock that was carbonate- and pyrite-depleted) (Jin and others, 2010) or as average bedrock (that is containing carbonate and pyrite) assessed from 9 to 15 m in the CZMW1 to 4 boreholes (Brantley and others, 2013). The deepest samples from boreholes CZMW1 and CZMW2 were not included because they apparently intersected the Keefer Sandstone unit (Brantley and others, 2013). In other words, in some cases, we have assumed parent is the saprock that already has lost its pyrite and carbonate, and in other cases the deepest unaltered material.

The relatively recent completion of the CZMW8 borehole provided additional deep material suitable for estimating parent material (table 8). The mean bulk geochemical composition of the deepest four samples from DC1 and CZMW8 were similar for most elements and were therefore averaged here to represent parent material. Samples from DC1 at 23 m and 24.5 m were excluded because their concentrations were particularly high in Ca, Mn and Fe and low in Al and K (> one standard deviation from the mean). We assume those layers are particularly carbonate-rich. Na and Mn average concentrations were slightly lower in CZMW8 compared to DC1 (table 8), where the standard deviation around the mean for parent material was 20 percent and 67 percent, respectively. Likewise, the standard deviations around mean Fe and Ca were calculated between 12 and 20 percent. In contrast, the standard deviation around the mean concentration was < 10 percent for all other elements. These uncertainties were used when propagating the calculated error for τ.

Scanning electron microscope (SEM).—Several samples from the CZMW8 core were imaged by scanning electron microscopy (SEM) using a FEI NanoSEM 630 FESEM microscope with an accelerating voltage in the range of 3 to 4 kV and a landing energy in the range of 2 to 3.5 kV under backscattered electron mode. Energy dispersive X-ray spectroscopy (EDS) was used to determine elemental compositions using an Oxford EDS detector; these values are reported here based on atomic percentages on the basis of anhydrous formulas. The effective beam size during each analysis was 2 to 3 μm.

RESULTS AND DISCUSSION:

The Stratigraphic Section

A synthetic stratigraphic section, developed from outcrop observations in the area, shows that the Rose Hill shale contains more interbedded sandstone and limestone near the contact with the Keefer Sandstone near the catchment outlet than down section to the east (fig. 1). Consistent with this, Keefer Sandstone cobbles and boulders on the land surface ("float") are observed along the westernmost portion of the catchment near the outlet (fig. 1; green triangles). LiDAR imagery also shows a topographic feature near the outlet of the catchment (dashed green line in fig. 1), coincident with the maximum uphill extent of the sandstone float. This lineament is attributed to the contact between the easily eroded Rose Hill shale and the more resistant Keefer Sandstone. Thus, the catchment is underlain entirely by the Rose Hill Formation except at the outlet where the stream crosses into the Keefer Sandstone.

Based on our observations outside the catchment and the strike of these strata (as indicated by the Keefer contour and the observations discussed below), we hypothesize that the increase in limestone bed thickness and frequency initiates ~ 65 m east of the Keefer Sandstone contact (plotted as a yellow line; fig. 1). Placement of the yellow line

is constrained by the measured section from the local area around Shale Hills and by the line on LiDAR attributed to the Keefer Sandstone (outlined in green; fig. 1).

Strike and Dip

The SSHCZO, located on the northwest-dipping limb of a 5 km wide northeast-plunging syncline in Silurian strata, is underlain primarily by steeply dipping shale of the Rose Hill Formation (Clinton Group). For example, dip measurements from the OTV data from the ridgetop boreholes at CZMW5, 6, 7 and 8 yielded a mean + 1 standard deviation of $52° ± 10°$ (see later discussion for fig. 2; OTV data available at criticalzone.org). Consistent with these measurements in ridgeline boreholes, the 58 measurements of dip (fig. 1) made in outcrops and pits in and around SSHCZO ranged from $40°$ to $88°$ ($64° ± 19°$) to the northwest. The Rose Hill Formation shale is characterized regionally as containing zones of meter-scale chevron folds, and some of the small-scale variations in dip are attributed to the likely presence of such features. In contrast, the overlying Keefer Sandstone (Clinton Group) is characterized regionally by monoclinal folds. The shallow dip angles (25–$30°$) in the sandstone beds observed in the OTV logs in boreholes at the catchment outlet (Kuntz and others, 2011) are therefore inferred to reveal the presence of a monocline at the mouth of the Shale Hills catchment (fig. 2).

Fracture orientations observed in and around the SSHCZO in outcrops or pits can be described as falling within three sets of orientations: i) parallel to bedding (striking WSW), ii) slightly oblique to bedding (striking ~WSW), and iii) perpendicular to both bedding and strike (striking ESE). Fractures trending perpendicular to bedding are more commonly observed in the more coherent sandstone and limestone interbeds, whereas the fractures subparallel to bedding are most common in shale beds.

Puck-shaped blocks, inferred to be sandstone, and white veins, inferred to be calcite, were observed in the CZMW1 to 4 OTV images underlying the valley near the weir (fig. 2, Kuntz and others, 2011) at 3 to 8 m depth. Elevated concentrations of calcium were observed in the drill core material from the same depths (Kuntz and others, 2011; Brantley and others, 2013). At 7 to 8 m depth under the valley, OTV images show a distinct change in color of strata from light brown to gray. This color change was observed with OTV at ~16 m on the south ridgetop borehole CZMW8.

Catchment Hydrodynamics

Groundwater table.—Groundwater levels from the 25 wells ranged from 0.8 m above the land surface to 26 mbls. Wells 6 to 11, located in the center of the catchment, often showed water levels above the land surface. During these periods, the groundwater levels from the unconfined water table in this portion of the catchment were greater than that of the stream and the stream is therefore a gaining stream. The deepest water table was observed in all wells between August and October (Appendix 2, table A2-1). In the valley floor wells 2 to 8, 10 to 11, 17 and CZMW1 to 4, the depth to the water table varied seasonally from 2.1 mbls to 0.8 m above the land surface (14 wells over different 11 months). Seasonal water table fluctuations were less evident in wells 3, 4, 7 and CZMW4 in the southwestern portion of the watershed (figs. 1, 3 and 4) where the apparent age of the groundwater was older (see groundwater age tracers below). The fairly constant groundwater temperature measurements at CZMW4 as compared to CZMW1 also support the presence of older groundwater at CZMW4 (Appendix 2, fig. A2-1).

Under the ridgetops, the depth to the groundwater table was observed from ~ 6 to 26 mbls, with the greatest depths observed in DC0 and CZMW8 drilled approximately mid-catchment (Appendix 2, table A2-1, figs. A2-1, A2-2, and A2-3). In contrast, groundwater levels were highest at the top of the catchment (boreholes CZMW5–7). The sharp contrast in the water table roughly between boreholes CZMW5 and DC0 (fig. 3) is therefore interpreted as evidence for a shallow permanent zone of interflow
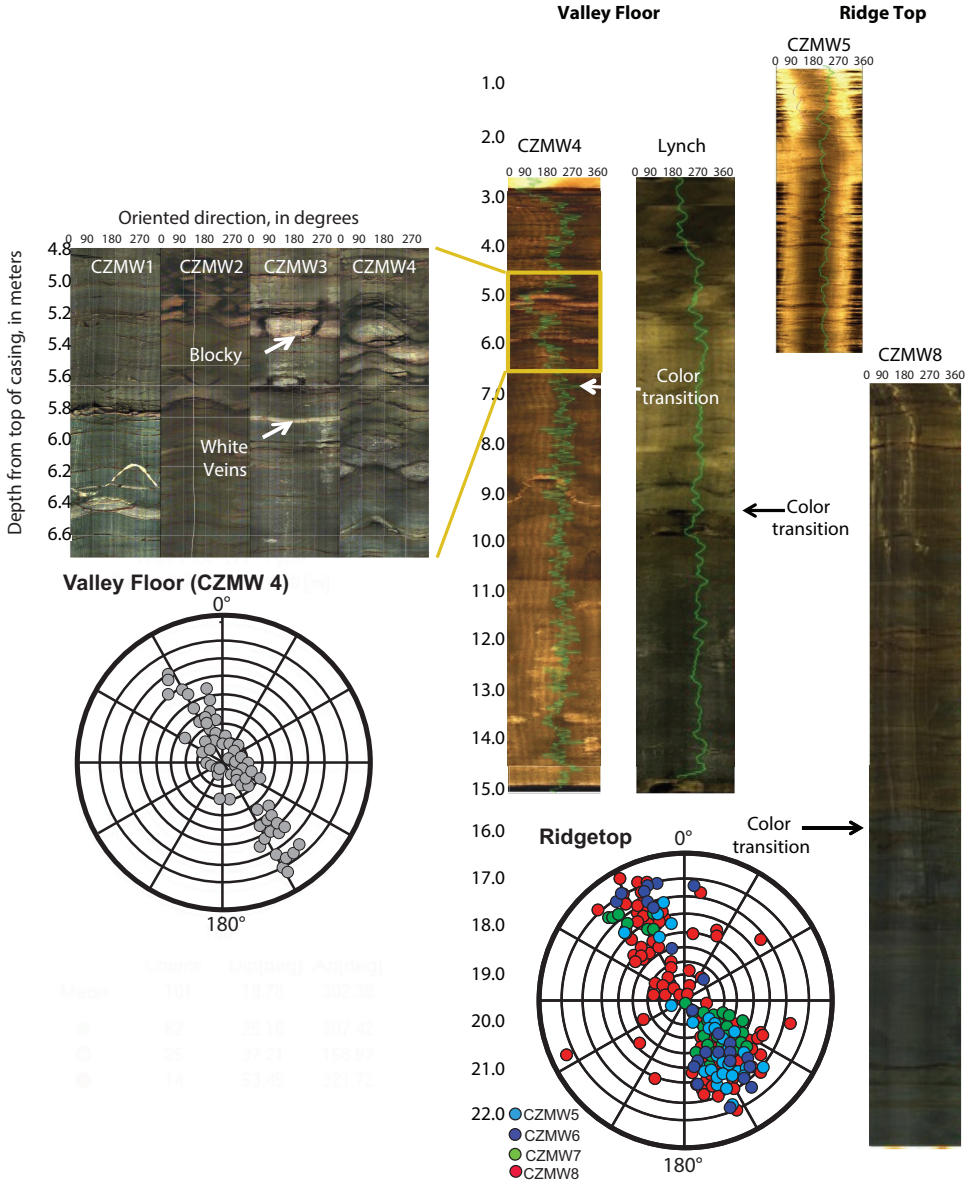
Fig. 2.   Stereo plots show fracture orientation and dip angle from OTV data; shallower dip measurements were observed in the valley floor (CZMW1-4 and lynch; stereo plot bottom left) compared to the ridgetop (CZMW5-8; stereo plot bottom right). Puck-shaped blocks and white veins were observed in boreholes CZMW1-4, while a distinct color change was observed in CZMW 1-4, lynch and CZMW8 boreholes at ~ 7, 9 and 16 m, respectively but not in CZMW5-7.

that is perched because of the contrast in permeability between the highly fractured zone in the upper meters and the more impermeable and less fractured zone beneath. This shallow permanent zone of interflow is measured in the eastern-most wells because the permeability barrier was not breached during drilling of those wells but was breached in CZMW8 and DC0 wells that were finished more than 12 m below the bottom of the fractured zone.
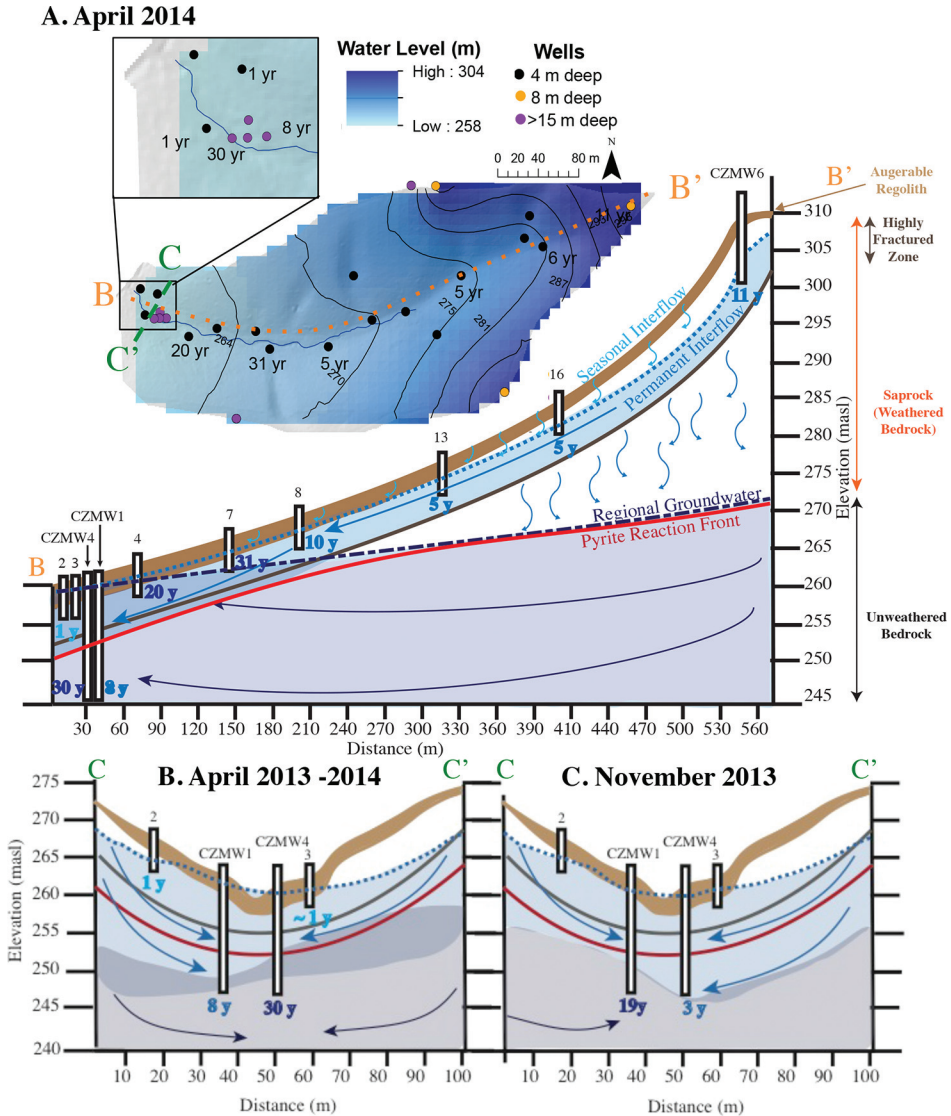
Fig. 3. (Top) The potentiometric surface at Shale Hills in April 2014 and the corresponding interpreted age at 10 wells based on the atmospheric tracer SF6. (Middle) Using groundwater levels, groundwater apparent ages, borehole optical televiewer data and bulk geochemistry, we constructed a conceptual diagram of subsurface water flow and pyrite oxidation. Under the uplands, most of the meteoric water infiltrates into augerable regolith and the highly fractured zone (5–8 mbls). This forms a perched saturated zone that allows water to flow laterally toward the channel as interflow. Some of this O_2-rich water also percolates down to the regional water table where pyrite oxidation is occurring. Under the valley floor, O_2-rich interflow penetrates below the channel pushing the pyrite oxidation front to ~8 m below the water table (Bottom). The depth to which interflow penetrates below the channel shifts seasonally. Here, interflow penetrates to a greater depth north of the channel when the catchment is saturated with water (winter and spring) as shown in the panel at the bottom left while the interflow penetrates to greater depth south of the channel when the catchment is dry (Summer-Fall) as shown in the panel at the bottom right.

The depth to water table roughly defines two directions of groundwater flow under the catchment. In the shale-rich zone east of interface A that constitutes the
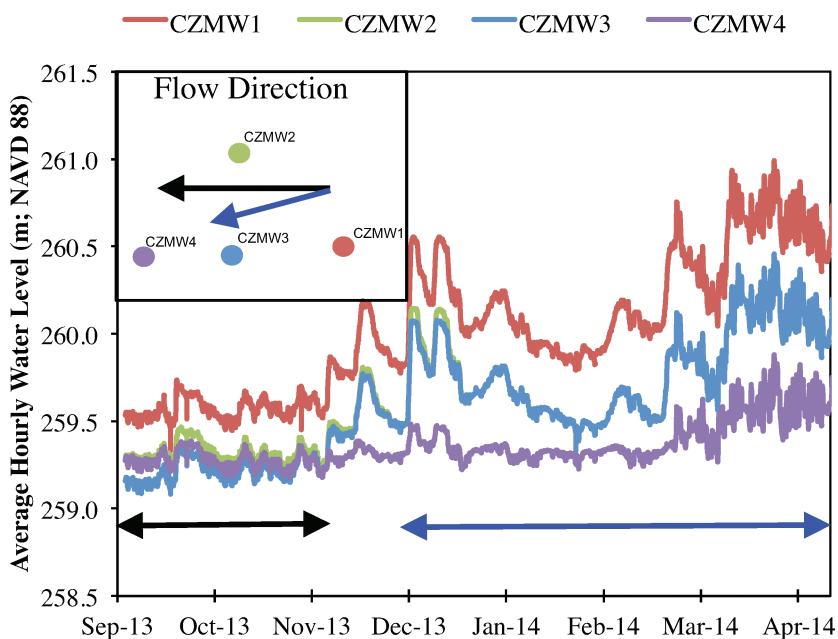
Fig. 4. Continuous groundwater levels (color) monitored at four wells near the outlet of the catchment support the direction of the groundwater flow indicated by potentiometric map (fig. 3). Arrows indicate predominant direction of groundwater flow between CZMW1–4 between September-November 2013 (black) and December-April of 2013/2014 (blue).

lower part of the stratigraphic section (fig. 3), fractures are steeply dipping to the WSW and the hydraulic head gradients between the ridge and the central valley floor are consistent with groundwater flow toward the channel. This is consistent with the interpretation of a gaining stream between wells 6 to 11. In contrast, to the west of interface A in the zone with calcareous and sandstone interbeds, the dip angle changes to become shallower and the fracture orientation is both WSW and ESE. In this zone, groundwater flows predominantly westward out of the catchment into Shavers Creek (figs. 1 and 3).

Some seasonal variations were superimposed on these two overall groundwater flow patterns. Continuous groundwater level measurements from CZMW1 to 4 indicated that groundwater flowed westward at the outlet during relatively dry periods (for example summer through November; black in fig. 4) but more southwestward during the wet season (between December and April; blue in fig. 4). In other words, groundwater flow in the lower part of the watershed was directed toward the stream during wet periods when the water table under the ridges was higher, and was directed to the west in line with regional topographic gradients during dry periods when the water table under the ridges was lower. Such behavior in an upland watershed is common: local flowpaths dominate under high-water conditions while regional flowpaths dominate under low-water conditions (Gleeson and Manning, 2008).

Groundwater age tracers.—When analyzed with the piston flow model, groundwater ages estimated based on SF_6, CFCs and tritium collected from CZWM1–4 in April 2013 were in good agreement and consistently <40 years old (table 2; Appendix 1). We focus the discussion on the piston flow apparent ages from SF_6 because these data provide a better resolution of the watershed. From November 2013 and March 2014, SF_6 concentrations were consistent with residence times from <1 to 30 years (fig. 3,

table 2). The SF_6 concentrations near the channel outlet vary substantially within a short spatial distance with much younger water in CZMW1–3 (on the north side of channel; 9–15 mbls) as compared to CZWM4 (south side, ~15 mbls). Apparent ages range from ~ 4.5 to 9 years versus ~35 years in those wells, respectively. This strong spatial gradient in groundwater flow ages near the channel outlet is consistent with the interpretation that the stream is gaining from convergence of multiple groundwater flowpaths each with different ages. In such a channel, the oldest waters are expected closest to the center of the stream (Modica and others, 1998). This behavior has been documented using CFCs and ^{3}H in large watersheds underlain by unconsolidated material (Böhlke and Denver, 1995; Böhlke and others, 2002; Kennedy and others, 2009; Gilmore and others, 2016;) and in an alpine crystalline fractured rock system (Manning and Cain, 2007).

In addition to these spatial variations, the tracers from CZMW1 and CZMW4 revealed that groundwater age substantially varied with season. Specifically, during the dry season when westward regional groundwater flow was dominant at the outlet, older water was observed on the northern side of the stream (CZMW1, ~19 y old) as compared to the southern side (CZMW4, ~3 y old). In contrast, during spring 2013 and 2014, when the hydraulic gradient between ridge tops and valley were greatest, local groundwater flow patterns were dominant and younger water was observed on the north as compared to the south side. Large variations in age (5–10 y) have similarly been observed between annual sampling events at multiple wells in the Sagehen Basin, located in the Sierra Nevada Mountains of California (Manning and others, 2012). In that instance, snowmelt correlated with younger water.

In general, the apparent age of the groundwater increased downstream, consistent with the conceptual model of groundwater flow in upland catchments (Modica and others, 1998). Specifically, the apparent age for groundwater at 4 mbls from upstream (wells 8, 13 and 16), ~5 y, was younger than samples from downstream in the southwest portion of the catchment (wells 4 and 7) where the apparent age was estimated at ≥ 20 y for the same depth (fig. 3). These data are used to infer the following generalizations: 1) water flows largely as interflow toward the channel in the uplands with a residence time in the subsurface that is <5 y; 2) some water infiltrates from the bottom of this interflow to the regional water table throughout the catchment and then flows slowly as saturated-zone flow to the valley-floor; and 3) near the outlet, the shallower angle of dip and bedding-parallel fractures as well as the bedding-orthogonal fractures allow the regional older groundwater to emerge at depths shallower than 4 mbls west of line A (fig. 1).

The seasonal variability in water table fluctuations support these generalizations. Specifically, water levels are more variable (from 0.8 to 2.7 m) in upstream wells 8, 13 and 16, as expected if they access water with short residence times and were more controlled by meteorological conditions. In contrast, little seasonal variation was observed in the downstream wells 4, 7 and CZMW4.

We could only sample one ridgetop well (CZMW6) for tracers due to the inability to continuously pump groundwater from the other ridgetop wells. At CZMW6, the groundwater level (average ~5.5 mbls) varied seasonally (~3 m) and showed an apparent age of ~10 y. Given that CZMW6 is a ridgetop well completed to 7.5 m depth at the head of the catchment, we assume water in this well experiences a downward vertical flow gradient. Therefore, the age likely does not represent a mean groundwater time under the ridges but rather the age near the water table.

Overall, this distribution of ages indicates that interflow water (<5 yrs) predominantly recharges the stream in the eastern portion of the catchment, while interflow and regional groundwater mix under the valley to explain longer residence time measurements (> 20 yrs) where the sandstone and limestone interbeds are more

prominent. This locus of interflow and regional groundwater flow convergence may be pushed seasonally from north to south by seasonal changes in the hydraulic head between the ridgetops and valley.

Spatial Groundwater Geochemical Patterns

The groundwater patterns described in the previous section are consistent with spatial and temporal variability in geochemistry. Specifically, DO concentrations in the groundwater at the bottom of the wells (fig. 5A) ranged from 0.1 to 10.7 mg L^{-1}, but showed a distinct change between wells 7 and 8 near line A in figure 1. In comparison, water in equilibrium with the atmosphere at 10 °C is 11.3 mg L^{-1}. Consistent with the inferred influxes from deep groundwater in the zone west of line A, DO concentrations there were lower than 6 mg L^{-1}. Consistent with interflow as the source of most water in the upland areas (wells 8–13), DO concentrations tended to be higher east of this line. Interestingly, this pattern in DO is consistent with patterns in groundwater sulfur isotopes (Jin and others, 2014): isotopic values indicating pyrite-derived S were observed in half of the groundwater wells to the west of well 8 but not in other wells. In other words, lower DO values may be caused by pyrite oxidation in the slow-flowing groundwater into the more western wells.

Measured DO also correlates negatively with dissolved Mg^{2+} in the groundwater under the valley floor (fig. 5B) and positively with SF_6 (fig. 5C). This is consistent with influxes of older, O_2-poor and Mg^{2+}–rich waters at depth in the western portion of the catchment (see discussion of chlorite, below).

Dissolved oxygen, pH, conductivity and temperature varied seasonally in the groundwater as a function of depth at the outlet of the catchment (Appendix 2), revealing patterns generally consistent with the previously discussed shifts in local versus regional groundwater flow patterns and apparent ages. For example, trends in DO concentration were distinct between CZMW1 (north of channel) and CZMW4 (south of channel, fig. 6). South of the channel (CZMW4), DO consistently decreased with depth with generally lower DO during wet as opposed to dry periods. In contrast, north of the channel, CZMW1 showed either increases or decreases with depth depending upon season. In addition, elevated DO levels were observed during dry periods. These findings together with water table measurements and groundwater age are consistent with the interpretation that during the wet portion of the year, the high water table on the north hillslope drives older, O_2-poor groundwater to upwell south of the channel while younger interflow water recharges the groundwater north of the channel. In contrast, when the hydraulic head is reduced during the dry season, the locus of older groundwater upwelling migrates north and lowers the observed apparent age and DO concentrations of the groundwater north of the channel, while interflow becomes the dominant input south of the channel (fig. 3).

Spatial trends in major ion concentrations (fig. 7) are consistent with apparent groundwater ages and DO concentrations from samples collected at well bottoms. However, these ion concentrations also change as a function of depth. For example, the dissolved concentrations of the carbonate mineral-derived elements, Ca and Sr, were most elevated in the groundwater at the catchment outlet as compared to the ridgetop (fig. 7C). In contrast, groundwater concentrations of clay-derived elements (K, Mg, Si; fig. 7) measured in samples from the bottom of the wells were more elevated at the ridgetops as compared to the rest of the basin. Consistently, the lowest concentrations of all elements considered together were observed in the central valley, where the groundwater hydraulic head measurements were consistent with a gaining stream, DO concentrations were high, and the apparent age of the groundwater was young (fig. 7). The general picture which emerges is that clay dissolution dominantly controls the geochemical signature of the interflow water found in the oxic unsaturated zone high in the watershed, while carbonate dissolution dominates water
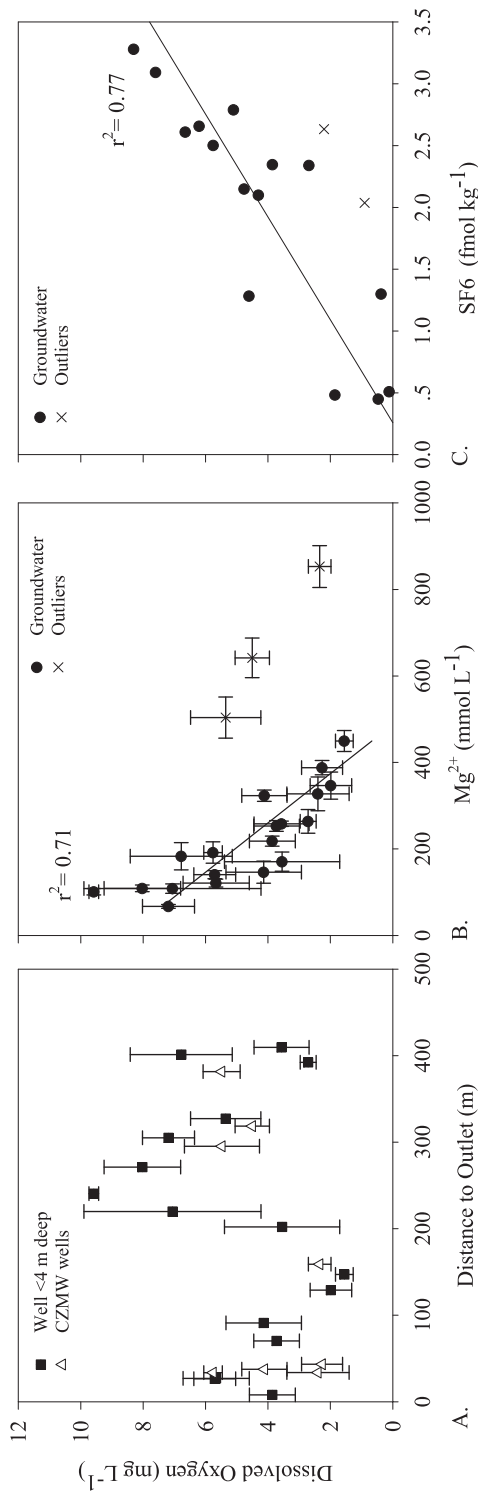
Fig. 5. (A) Groundwater dissolved oxygen concentrations averaged at each well across the catchment. (B) Average groundwater dissolved oxygen concentrations were inversely correlated with Mg^{2+} values, excluding CZMW5&6 and well 13, which had the highest Mg concentrations detected in the catchment. (C) Individual SF6 samples, used to determine water age, were positively correlated with *in situ* dissolved oxygen concentrations (x denotes DO non-*in situ* measurements) suggesting younger water had higher dissolved oxygen concentrations.
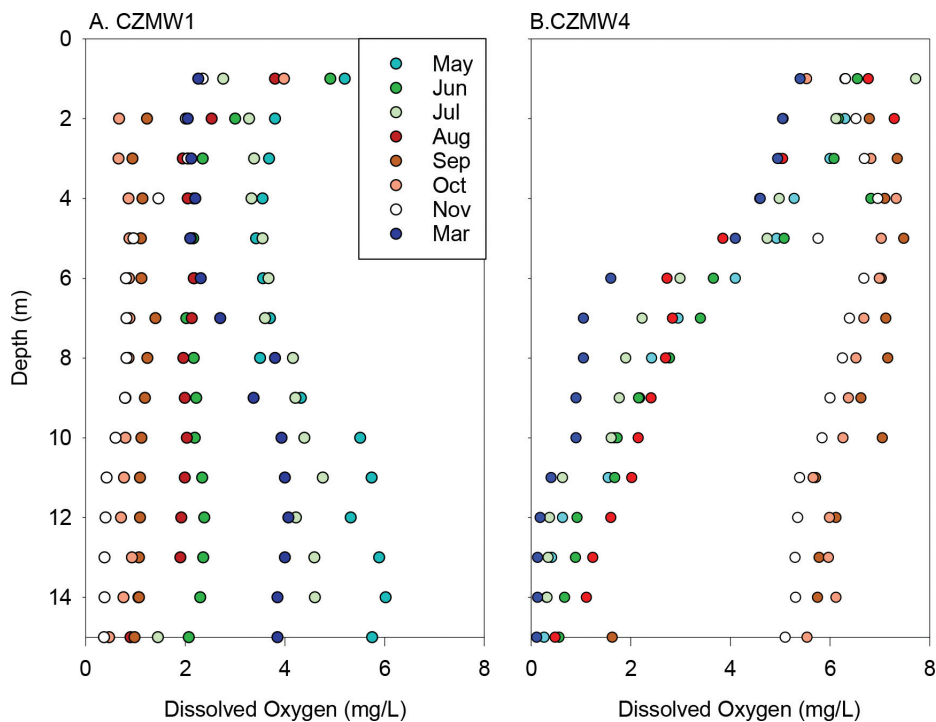
Fig. 6.   Groundwater dissolved oxygen concentrations observed over time in two boreholes lining the stream at near the watershed's outlet.

chemistry in the low-DO saturated zone at depth and lower in the watershed. The lower DO of this latter water is also consistent with pyrite oxidation.

Groundwater was consistently undersaturated (SI values < -0.05; table 4) with respect to calcite. The only exception was one instance in well 2 and three instances in CZMW1 near the outlet: both sites in February 2013 and CZMW1 in October and November 2013 were supersaturated with respect to calcite. Thus, the subsurface under the valley is mostly a source of dissolved carbonate and only occasionally is carbonate precipitating under the valley today.

Stream Water Chemistry

When present, stream water was sampled along with groundwater. Stream water pH varied from 5.7 to 7.1 over the study period, with near-neutral values dominantly during the growing season (April-October). The conductivity of the stream water averaged 62 μS cm^{-1} but increased during extremely low water levels (for example, October 2013, 203 μS cm^{-1}). The average stream concentration of most anions (HCO_3^-, Cl^- and SO_4^{2-}) and cations (Ca^{2+}, Mg^{2+}, Na^+, K^+) at the outlet were similar to shallow groundwaters in the central portion of the valley (that is, wells 10 and 11; table 3). The most elevated stream water concentrations were observed during the drier season generally from May to October, overlapping with the growing season. Si concentrations tended to show the same pattern as other dissolved ions. A more detailed examination of surface water solute behavior for SSHCZO can be found in Herndon and others (2015) and Bao and others (2016).

Average Groundwater Concentrations

A. Magnesium
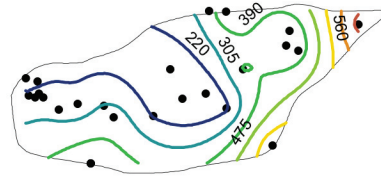
B. Potassium
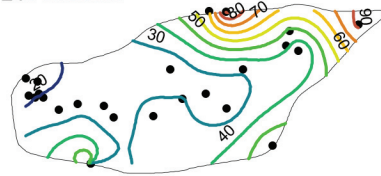
C. Calcium
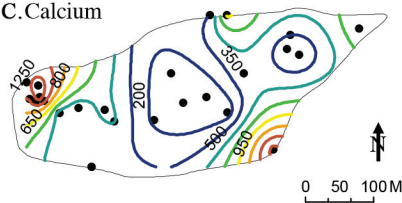
Fig. 7. Annual average groundwater concentrations (μmol L^{-1}; warm colors indicate high concentrations, cool colors indicate low concentrations) collected at the bottom of the wells for (A) magnesium, (B) potassium and (C) calcium. Wells ranged from 4 m to 50 m deep (see fig. 1).

Regolith Weathering and Mineralogical Analysis

Pyrite distribution.—Bulk sulfur concentrations were extremely low in recovered material (<0.01 wt%) at all depths in wells CZMW 5 to 7 (total depth 7.5 mbls) near the head of the catchment. Similarly low concentrations were observed in CZMW8 at depths shallower than 15 mbls (table 8; fig. 8B). As pyrite (FeS_2) is the only primary mineral that contains sulfur within the catchment (Jin and others, 2010, 2011), these data are consistent with a pyrite-depleted zone in the upper part of the catchment that was previously inferred in CZMW1-4 and DC1 (Brantley and others, 2013). For example, pyrite concentrations increased 100-fold from 15 to 30 mbls in CZMW8 (fig. 8B). The change at ~15 m was concurrent with a transition from dominantly ferric iron toward the surface (Fe^{3+}; less than 15 mbls) to dominantly ferrous iron (Fe^{2+}) at depth (table 8). The pyrite depletion zone is attributed to oxidative dissolution of pyrite that allows loss of S but retention of oxidized Fe in the upper meters of the catchment. Consistent with this, low concentrations of FeO (<1.8 wt%) were also measured in the entire depth interval of the relatively shallow CZMW5–7 wells.

The pyrite dissolution front was also documented in CZMW8 using SEM-EDS. At depth, pyrite occurred as fine-grained clusters of small octahedral pyrite grains (pyrite framboids) (fig. 9A). In samples devoid of all or partial pyrite, we observed Fe oxide/hydroxides in hexagonal rosette-like structures. These were observed in pores in every sample above the pyrite oxidation front in CZMW8 (fig. 9C). A similar but more poorly structured Fe oxide/hydroxide material was observed to coat chlorite surfaces (fig. 9D). Fe oxide/hydroxides were also observed in fractures and veins at 5.5 mbls. The depth interval over which pyrite is depleted was constrained to 1.1 m in
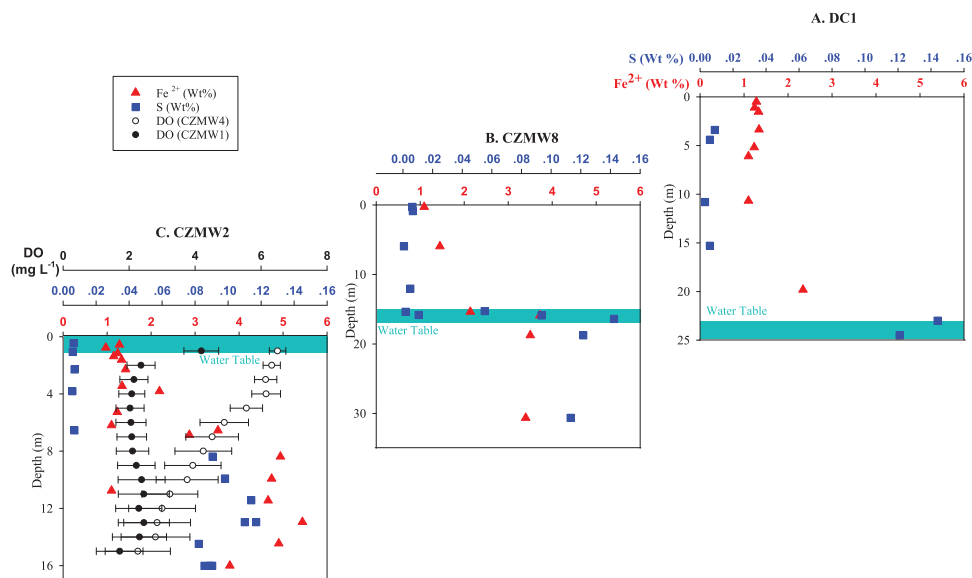
Fig. 8. Sulfur (S) and ferrous iron (Fe^{2+}) from three boreholes across the catchment: (A) DC1, (B) CZMW8, and (C) CZMW2. The average and standard error of the DO (mg L^{-1}) from CZMW1 and CZMW4 (fig. 6), located $\sim$ 5 m north and south of CZMW2, are superimposed on the CZMW2 profile.

thickness based on the change in bulk sulfur concentrations between 15.3 and 16.4 mbls in CZMW8. This front thickness was very similar to the depth interval, 1.4 m, where we observed the fluctuations of the water table (fig. 4).

Pyrite oxidation occurs when the mineral surface is exposed to water and a chemical oxidant such as O_2, Fe^{3+} or NO_3^- (Moses and Herman, 1991; Bonnissel-Gissinger and others, 1998; Ayraud and others, 2006). Given the very low NO_3^- concentrations observed at SSHCZO (< 30 μmol L^{-1}; table 3), this oxidant is unlikely to be important. Furthermore, groundwaters at SSHCZO are circumneutral in pH (averaging 6.4 and rarely dropping below 5.4); thus we do not expect Fe^{3+} to be the dominant oxidant due to the extremely low solubility of ferric minerals. Under these conditions, the following reaction is likely to govern pyrite oxidation:

$$15\,O_2 + 4FeS_2 + 8H_2O \Leftrightarrow 2Fe_2^{+3}O_3 + 8SO_4^{2-} + 16H^+ \tag{1}$$
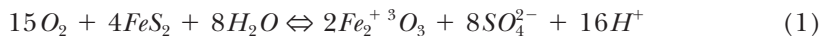
In other catchments, the pyrite oxidation front has also been observed to be roughly coincident with the depth interval of water table fluctuation (Ayraud and others, 2008). In that zone of fluctuation, air and water enters pore spaces intermittently, allowing oxidation. This mechanism is consistent with the general coincidence of the pyrite oxidation front with the water table at depths of 23 m under the northern ridge at and at ~15 mbls under the southern ridge at CZMW8. Likewise, although the pyrite reaction front was not reached in the 7.5-m deep CZMW5 to 7 wells in the uppermost part of the catchment, lack of pyrite in those boreholes is consistent with high O_2 concentrations above the water table.

In contrast, in the valley floor, the water table was never deeper than ~1 mbls (Appendix 2, table A2-1) whereas the depth of pyrite depletion was observed at ~8 mbls (fig. 8C; Brantley and others, 2013) and sulfur isotopic evidence was consistent with pyrite oxidation west of well 8 (Jin and others, 2014). In both valley floor wells CZMW1 and CZMW4 (fig. 8C) the lowest DO concentrations were observed deeper
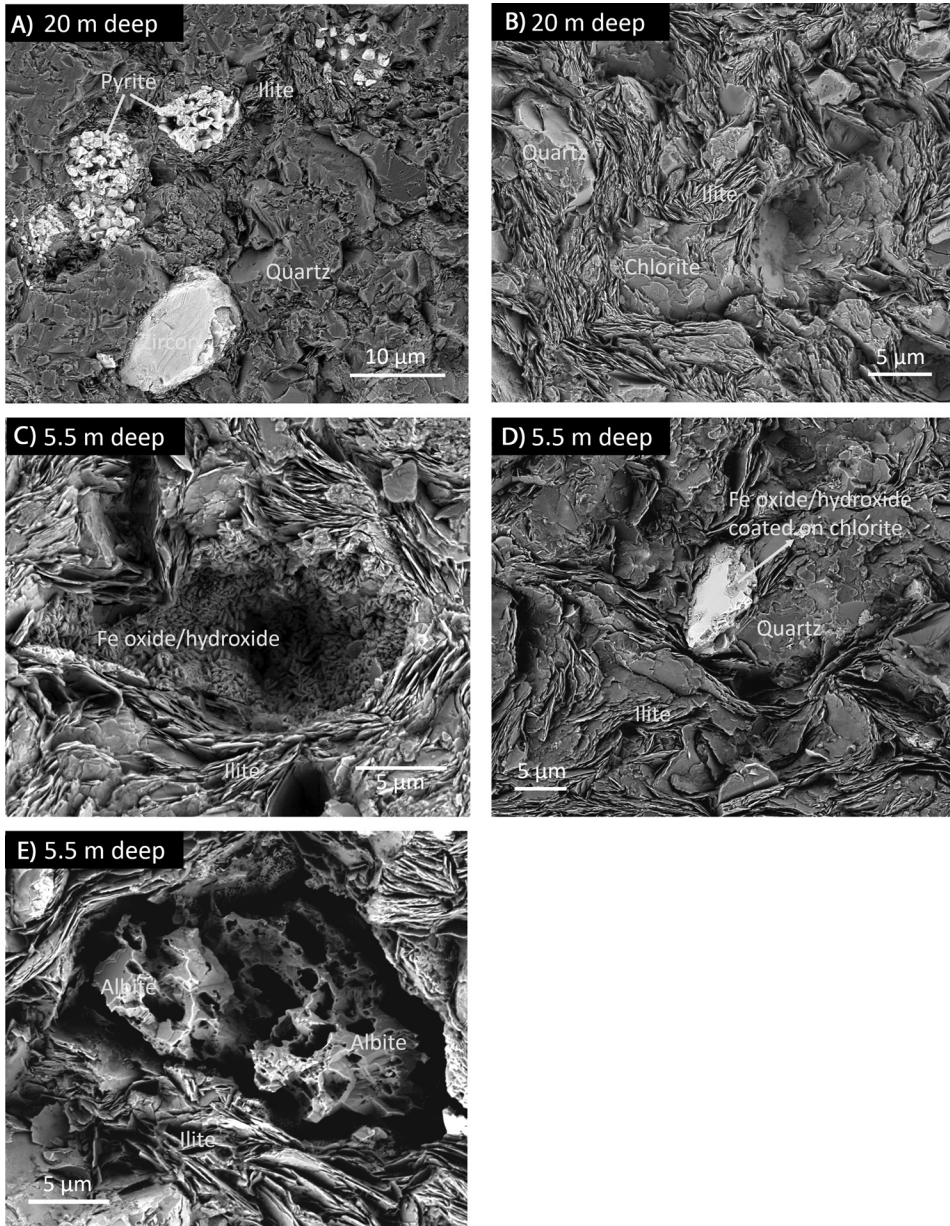
Fig. 9. Backscattered electron (BSE) image for samples from drilled core CZMW8: (A and B) unweathered bedrock from 20 m BLS showing presence of pyrite framboids (A) and chlorite and illlite (B) minerals, and (C, D and E) weathered bedrock from 5.5 m BLS showing development of secondary porosity (C and E) and formation of iron oxides in the pores and coating of chlorite minerals (C and D).

than 6 mbls, which is roughly consistent with the depth of pyrite depletion. We interpret these O_2-depleted waters to contain groundwater from beneath the ridge. From March through July we infer that O_2-charged interflow water flowed to depths greater than the pyrite reaction front north of the channel, while from September

though November, O_2-charged interflow water penetrated to depths greater than the pyrite reaction front south of the channel.

   Carbonate distribution and isotopic composition.—Ca, relatively low and variable in concentration throughout the catchment, has been observed in SEM-EDS to mostly be present as calcite ($CaCO_3$) or as Mg, Fe-containing carbonate (either ankerite or dolomite). For example, samples from CZMW1–4 contain calcite whereas samples from 23 to 24 mbls in DC1 contain $Ca(Mg, Mn, Fe)(CO_3)_2$ (Jin and others, 2010; Brantley and others, 2013). Sr isotope ratios are also consistent with the presence of ankerite in DC1 at depth and ankerite and calcite in CZMW2 (Meek and others, 2016). Conversely, carbonate minerals were not detected using x-ray diffraction (PANalytical Empryean X-Ray Diffractometer) in CZMW8 at depths of ~9 and ~29 mbls and thus are present at less than a few weight percent. Such variations are consistent with stratigraphic variations in total carbonate in the Rose Hill Shale throughout central Pennsylvania.

   The lowest Ca concentrations were generally observed near the land surface where calcite and ankerite were absent (shallower than 2 mbls in the valley or 15 mbls on the ridgetops) (tables 5–8). For example, Ca concentrations in the shallow boreholes CZMW5 to 8 were low, generally ranging from 0.02 to 0.14 weight percent. Given that the cation exchange sites were dominated by calcium (Jin and others, 2010), the trace Ca in shallow samples was likely present in illite or on exchange sites on other minerals.

   We estimated the average Ca concentration of the parent to be 0.12 ± 0.02 weight percent (table 8). In comparison to this parent, the calcium concentration in drilled material sampled from shallower than 15 mbls at CZMW5–8 showed depletion ($-0.90 < \tau < -0.14$; tables 5–8). Likewise, samples measured deeper than 15 m in CZMW8 were slightly more enriched in calcium ($-0.50 < \tau \leq 0.57$) than those measured coincident with or above the water table at 15 m ($-0.53 < \tau \leq -0.14$). We argue that in this eastern portion of the catchment where carbonate interbeds a rare, carbonate concentrations are extremely low but nonetheless consistent with inferred depletion of carbonate to the depth of the regional water table.

   Depletion of carbonate has also been documented in the valley floor boreholes to 2 mbls and to ~20 mbls in the northern borehole DC1 (Brantley and others, 2013). Thus, although not as clear as the depletion observed in DC1 and CZMW1–4, lower Ca in surface material in the eastern part of the catchment is thus consistent with near-surface carbonate depletion (Jin and others, 2010, 2011; Brantley and others, 2013).

   Brantley and others (2013) hypothesized that some of the calcite under the valley floor also formed as precipitation from upwelling groundwater. This hypothesis is consistent with the oversaturation of the waters for a few samples reported here although we observed no evidence for extensive carbonate precipitation (table 4). Consistent with the hypothesis that carbonate precipitates under the valley, isotopic measurements of ^{13}C reported previously (Brantley and others, 2013; Meek and others, 2016) documented more than one episode of carbonate formation. First, the interbeds of ankerite that increase in density toward the outlet (westward from line A in fig. 1) are likely primary carbonate precipitated during the Silurian based on the ^{13}C isotopes (-2.9 to -14.4 ‰; Brantley and others, 2013). This ankerite was reported in deep samples from boreholes DC1 and CZMW2. In contrast, Brantley and others (2013) measured C isotopes in carbonate near the surface in the CZMW2 borehole that are typical for carbon originating from organic material (OM). Therefore, the isotopic evidence is consistent with a second episode of carbonate precipitation where C was incorporated from OM in the original shale or more recent sources. Consistent with a second episode of carbonate precipitation that incorporates carbon from OM,

the isotopic composition of bulk total carbon in some samples from the CZMW7 and CZMW8 boreholes [approximately -23.9 ‰ (table 10)] was relatively constant and much more depleted.

Mineral reactions from the saprock to soil zones.—Na. Above 5 m, plagioclase grains were only rarely observed in samples under SEM. Between 5 and 20 mbls, albitic plagioclase grains in CZMW8 core began to exhibit etch pits, consistent with mineral dissolution across this depth interval (fig. 9E). Consistent with these SEM observations, concentrations of Na, found predominantly in albite (Jin and others, 2010), were depleted compared to Zr in the protolith ($-0.64 < \tau$) over the full extent of the north and eastern ridgetop boreholes (CZMW5-7; 7.5 m deep), and in the southern ridgetop (CZMW8) shallower than 12 m. These observations were interpreted to indicate the presence of a plagioclase reaction front extending from 5 to 12 m.

K. SEM was used to identify clay minerals in the CZMW8 core using morphology and composition from EDS. Illite was always observed as platey particles, often surrounding rigid particles like quartz or pyrite (fig. 9B). Platey particles were identified as illite under EDS by the characteristic Si/Al, K/Al and Mg/Al molar ratios of 1.32 ± 0.08, 0.28 ± 0.02, and 0.08 ± 0.02, respectively (Appendix 3). Utilizing a normative model (see Appendix 3 for details), the calculated composition of illite in the parent rock is $K_{0.69}(Si_{3.24}Al_{0.76})(Al_{1.69}Fe^{3+}_{0.10}Fe^{2+}_{0.16}Mg_{0.19})O_{10}(OH)_2$. The element ratios for the platey illite particles under EDS were the same in all samples of rock chips (>2 mm) recovered from drill cores or soils when observed under SEM EDS (Appendix 3, table A3-2).

Although the K/Al ratios are constant in the rock fragments, we observed lower K/Zr ratios in the digested bulk material in samples down to a depth of 8 m in CZMW8 and especially in the augerable soil (Appendix 3). Such loss of K compared to Zr can be attributed to both loss as particles and loss as solute. In fact, K- and Al-containing particles are known to have preferentially mobilized compared to heavier zircons in this catchment (Jin and others (2010). Specifically, illite particles in the < 2 mm size fraction (Appendix 3, table A3-2, fig. A3-1) may be preferentially lost from the soils and saprock, lowering the K/Zr ratio. In contrast, loss of more K than Al documents partial solubilization of K as compared to Al in the fines. Given these observations, K (illite) is lost mostly as particles, and K is only solubilized to any extent in the augerable soil.

Mg. In contrast to the consistently platy illite particles, "chlorite" from the drill core was identifiable under SEM as irregularly shaped particles. SEM-EDS quantification of "chlorite" indicated a constant Si/Al ratio over the whole depth range analyzed in CZMW8 (that is, 0.1 to 15 m, Appendix 3, table A3-1), but the Mg/Al ratio decreased upward from $\sim 0.32 \pm 0.05$ to $\sim 0.21 \pm 0.05$. Thus we infer that Mg was lost relative to Al in the "chlorite" between depths of 0.1 and 15 mbls.

Consistent with this, bulk Mg concentrations in the ridgetop boreholes (CZMW5-8) at depths less than 10 m were depleted compared to Zr in the protolith ($-0.72 < \tau$). Only borehole CZMW8 reached a depth where values were consistent with parent composition (tables 5–8; fig. 10). When Mg:Zr ratios were examined for CZMW8 samples with depth, the trend suggests Mg depletion persisted to a depth of ~ 15 m, roughly coincident with the water table position and pyrite oxidation. Thus, the Mg depletion in the upper parts of these boreholes is attributed to the solubilization of Mg from "chlorite" starting at depths of ~ 15 mbls, illite particle loss beginning at ~ 8 mbls (tables 5–8; fig. 10) and finally illite solubilization beginning in the augerable soils.

To determine the nature of this reaction we compared Fe(II):Al and Mg:Al ratios observed in the drill core material (fig. 11). The positive relationship between these ratios is consistent with oxidative weathering of Mg-rich clay minerals to transform Fe(II) to Fe(III) with accompanying loss of Mg to maintain charge balance. At SSHCZO, these clay minerals are illite and "chlorite". Utilizing the ratio of Mg/Al
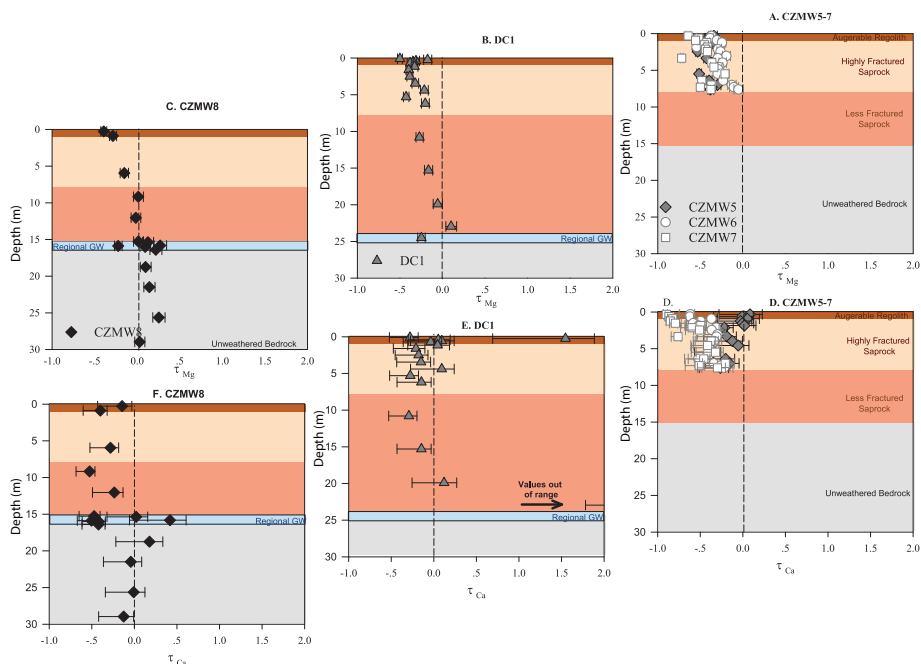
Fig. 10. Values of τ_j for j = Mg (A–C) and calcium (D–E) from ridgetop drill core material in CZMW5–7 (A and D), DC1 (B and C), and CZMW8 (C and F). Values < 0 indicate depletion compared to parent material, while values > 0 indicate enrichment compared to the parent material.

obtained from SEM, we observed a quantifiable decrease in the Mg:Al ratio in the "chlorite" toward the land surface, while the chemical composition of illite remained almost constant. Consistent with this, the irregular shape of the chlorite minerals observed via SEM suggests weathering is occurring in a sheet-by-sheet mechanism as the mineral moves toward the land surface, whereas the platey geometry of the illite documents little to no such deep reaction. We therefore argue that the loss of Fe(II) is due to chlorite oxidation, which is accompanied by the loss of Mg^{2+} to the aqueous solution for charge balance.

The weathering products of chlorite are likely vermiculite or hydroxy-interlayered vermiculite, Fe-oxide and aqueous Mg^{+2} (Lee and others, 2003). The deep reaction of chlorite to these products represents a newly discovered oxidation front at SSHCZO, though one that has been observed in other weathering sequences (Johnson, 1964; Bain, 1977; Ross and other, 1982). For example, Proust and others (1986) documented chlorite oxidation (also termed supergene vermiculitization of chlorite) in amphibole schist from an outcrop in Longes, France. In their detailed analysis, they also found a progressive loss of Fe^{2+} and Mg^{2+} from the octahedral sites of the chlorite, which led to a slight Si/Al enrichment.

Utilizing a normative model (Appendix 3), the calculated composition of average "chlorite" in the parent rock is $(Fe^{2+}_{0.40}Mg_{0.15}Al_{0.35})_6(Si_{0.76}Al_{0.24})_4O_{10}(OH)_8$. This composition (and the composition quoted above for illite) varies from those reported earlier by Jin and others (2010). Here, we only used the composition of the parent rock to derive the mineral composition, whereas in the earlier treatment, Jin and others included near-surface samples in which vermiculite and hydroxyl-interlayered vermiculite were present at higher concentrations. Utilizing the new stoichiometries, we write the average expression for the oxidation of chlorite as:
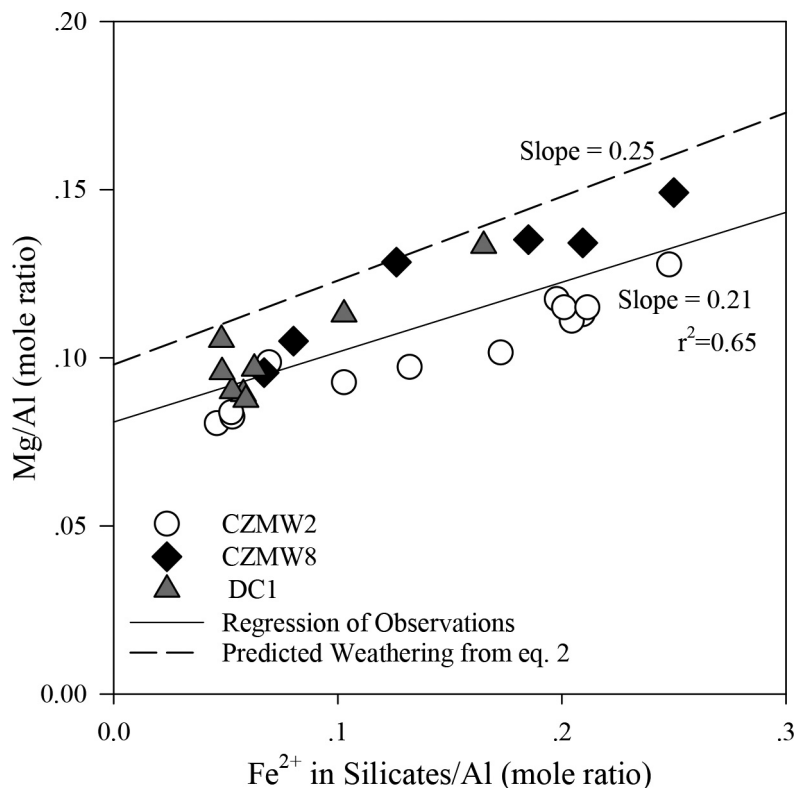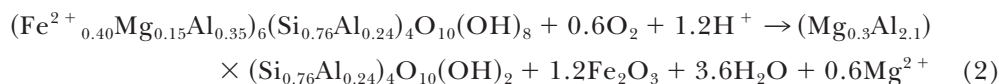
Fig. 11. Correlation (solid line) of Fe^{2+} in silicates versus Mg concentrations from the drill core material normalized to Al concentrations, compared to the Mg lost from chlorite oxidation based on equation 2.

$$(Fe^{2+}_{0.40}Mg_{0.15}Al_{0.35})_6(Si_{0.76}Al_{0.24})_4O_{10}(OH)_8 + 0.6O_2 + 1.2H^+ \rightarrow (Mg_{0.3}Al_{2.1})$$
$$\times (Si_{0.76}Al_{0.24})_4O_{10}(OH)_2 + 1.2Fe_2O_3 + 3.6H_2O + 0.6Mg^{2+} \quad (2)$$

This stoichiometry and amount of Mg release mirrors the trends observed in the drill core material (fig. 11) and can be used to quantify infiltration of water from the land surface to the water table, tens of meters below the ridgeline. Specifically, the reaction front for Fe^{2+} is wider under the valley floor than the corresponding sulfur front (fig. 8C). Thus, Fe oxidizes over a depth interval of tens of meters but pyrite oxidizes within a few meters. Consistent with this, the highest Mg and lowest DO is observed in waters with residence times of ~30 years at depths of ~15 m under the outlet. The chemical composition of these waters can be interpreted in the context of chlorite oxidation as in eq. 2. With this calculation, we infer a chlorite oxidation rate of ~ 9 μmol m^{-3} y^{-1}. In comparison, the estimated loss of chlorite per year based on the weathering advance rate observed in soils is ~1 mmol m^{-3} y^{-1} (Appendix 3).

INTERPRETATIONS AND IMPLICATIONS

Subsurface hydrologic flow is governed at Shale Hills by both the low primary permeability and porosity of the protolith and by the secondary porosity and permeability that develops as the protolith converts to regolith. As water moves through the catchment, the flowpath imposes a chemical fingerprint as the cumulative effect of

hydrobiogeochemical reactions. Under the SSHCZO, secondary porosity and permeability are developed due to physical fracturing and mineralogical reactions. The chemical reactions are generally localized in specific depth intervals which we call reaction fronts. In 3 dimensions the fronts are nested and subparallel to the land surface, although they cross under the valley. The identification of such nested reaction fronts can elucidate subsurface flowpaths and be used to improve catchment hydrogeochemical models (Brantley and others, 2016). Here, we refine this idea by combining contemporary groundwater hydrogeochemical data with drill core bulk geochemistry to interpret relationships among water flows, regolith production and landscape evolution. Below we describe a conceptual model of catchment evolution. Specifically we argue that the propagation of the deepest mineral reaction front (pyrite) under the valley enhances channel incision and thus the geomorphic evolution of the catchment.

Lithologic Controls on Groundwater Flow

Along with the other Paleozoic strata, the Clinton Group is strongly folded and faulted in the CZO. The density of fractures throughout the catchment is highest in the uppermost 5 to 8 m deep layer and the fractured layer is attributed to frost cracking and other periglacial processes associated with the LGM (Jin and others, 2010; Kuntz and others, 2011; Brantley and others, 2013). The eastern part of the catchment is underlain entirely by Rose Hill shale and is generally impermeable except for fractures. The fractures tend to be bedding plane openings that presumably have dilated during exhumation and that are steeply dipping. In the western part of the catchment, especially west of line A (fig. 1), sandstone and limestone and calcareous interbeds increase in frequency, and fractures are observed commonly to be both perpendicular to and parallel to bedding. In addition, because of the inferred presence of a fold near the outlet, bedding is observed to be almost horizontal under the catchment outlet. We infer that the hydraulic conductivity of the protolith is larger in the west near the valley, compared to the east near the upper ridges, with a marked change near line A (fig. 1).

The surficial fractured zone overlies less fractured rock and is inferred to saturate and act like a perched aquifer that allows water to flow downslope throughout the catchment as interflow. Much of the stream response is due to interflow. The perched layer also reduces infiltration of water into the underlying unsaturated zone and into regional or valley groundwater. East of line A, the dominant flowpath for interflow and regional groundwater is toward the stream, but in the less steeply dipping fracture network west of line A, both flowpaths are directed along a more westward regional groundwater orientation. During wet periods, groundwater flows dominantly toward the channel and during dry periods, it flows dominantly westward. Pathways of interflow throughout the catchment are thus largely dictated by the hydrostatic head and by physical factors, including characteristics of the stratigraphic section and periglacial fracturing.

Flow Paths and Nested Reaction Fronts

In addition to interflow, water also moves out of SSHCZO as deep groundwater. Shallow interflow and deep, regional groundwater flow are each marked by geochemical signatures based on the source of protons driving weathering (Jin and others, 2014): 1) interflow is delineated by silicate dissolution driven by protons from atmospheric-related and organic acids; 2) deep groundwater flow is delineated by Mg and Ca from carbonate dissolution driven by protons released by oxidizing pyrite and dissolved S from the latter reaction. Beneath the valley where the regional water table is very shallow, these flows mix and is imprinted by carbonate dissolution driven by

protons from atmospheric-related and organic acids. Below we discuss how these flowpaths may impact geomorphic evolution of the SSHCZO.

Interflow generally occurs within the highly fractured zone 5 to 8 mbls and thus has short residence times (<5 y). These dilute, oxygenated waters contain Mg derived from dissolution of "chlorite" and illite and Ca from rain. The characteristic Ca/Mg ratio of precipitation is 3.6:1. In the eastern portion of the catchment, interflow has Ca/Mg ratios of 1:1 due to preferential release of Mg from the clays imprinted on this rain signature. Under the central channel, interflow becomes indistinguishable from groundwater flow.

Compared to interflow in the eastern part, the waters within 4 mbls near the outlet at the western end of the catchment are (i) younger (~ 1 y), (ii) more elevated in solute concentrations, (iii) less rich in DO and (iv) higher in Ca/Mg ratio (approaching 10:1). In this part, the O_2-charged acid meteoric waters (average pH = 4.5; Herndon and others, 2015) dissolves Ca carbonate in the limestone interbeds at depths below 2 mbls.

Finally, the deep-flowing waters near the outlet of the catchment maintain stable water levels, are characterized by longer residence times, lower DO, and higher magnesium concentrations. These waters likely originated as recharge from the bottom of the interflow zone at depths of 5 to 8 mbls that has infiltrated deeper saprock to the regional groundwater table. A slight hydraulic head gradient from under the ridge to the valley drives this groundwater flow to the wells near the outlet. The flow direction changes from westward to southwestward seasonally between dry and wet periods.

Infiltration of some O_2-rich water to the regional water table is documented everywhere in the watershed that we have drilled by (i) secondary porosity, (ii) release of Mg from oxidizing chlorite, (iii) dissolution of carbonate, and (iv) oxidation of pyrite. Regional groundwater is thus O_2-depleted (fig. 5). Groundwater that has oxidized chlorite and pyrite along its flowpath emerges in the subsurface at the outlet of the catchment with low DO at the depth of the pyrite front in the north in CZMW1 during the dry summer and in the south in CZMW4 during the wet season. The low DO in this water does not promote fast pyrite oxidation under the outlet. Therefore, during the wet season when water flows predominantly toward the channel, oxidation of pyrite is faster under the north side of the stream (CZMW1) as compared to the south side (CZMW4). In contrast, during the dry season when the overall flow is westward, this O_2-depleted water is no longer observed in the well at depth south of the stream (CZMW4). Apparently, as the catchment dewaters due to high rates of evapotranspiration in the summer, groundwater flows predominantly to the west and oxidation of pyrite is faster under the south side of the stream (CZMW1) as compared to the north side (CZMW4). Seasonal pumping thus results in the depth of deepest incision varying from north to south under the channel.

Chemical Incision and Geomorphological Evolution

According to these arguments, seasonal pumping controls mixing of O_2-rich groundwater and oxidative weathering in the bedrock under the channel. Over time, the O_2-rich shallow groundwater oxidizes pyrite to produce sulfuric acid (H_2SO_4), which then dissolves carbonate minerals and opens secondary porosity. This small enhancement of porosity under the channel may in turn weaken the rock and slowly enhance channel incision.

The rate of groundwater flow is a function of the storage, recharge rate, permeability, and hydraulic gradient, where storage is a function of porosity (Fetter, 2000). Thus, the enhancement of storage at depth under the channel by oxidative dissolution of pyrite will also cause the water table near the channel to drop. In turn, the lower water table near the channel will enhance the hydraulic gradient between the ridge tops and

channel, driving drainage from the watershed. When considered over geological timescales, such drainage could control the rate of weathering advance under the entire catchment (Rempe and Dietrich, 2014). As a conceptual model, we therefore propose that channel incision is enhanced by pyrite oxidation. As oxidation proceeds, the water table under the channel lowers, which then promotes drainage and lowers the water table higher in the watershed. Lowering of the water table away from the channel in turn allows for enhanced infiltration of oxygen- and acid-rich water deeper into the bedrock, propagating the depth of the deepest reaction front under the catchment uplands.

<div align="center">CONCLUSION</div>

To explore the structure and dynamics of critical zone evolution, we defend a conceptual model for the interplay between regolith evolution and hydrodynamics in a small, upland watershed in the northeastern U.S.A. The position of the water table is governed by the distribution of secondary permeability in the watershed that developed from biogeochemical reactions and periglacial fracturing combined with the distribution and structure (strike and dip) of primary permeability related to the stratigraphic section of the underlying clastic rocks. In the upland eastern portion of the catchment, lower-permeability, steeply dipping shale hosts a high, perched water table that is characterized by interflow to the channel, whereas in the western portion the higher hydraulic conductivity strata allows more regional flow. Throughout the watershed, two main flowpaths are easily identified based on chemical signatures: 1) O_2-rich and shallow interflow comprises most of the stream water and carries most of the weathering elements out of the catchment; and 2) O_2-poor deep groundwater contributes to the stream near the catchment outlet and originates from meteoric water that infiltrated to the regional water table because it was not captured into interflow. This latter water travels from land surface to deep groundwater removing Mg, Ca, and S from the catchment due to reactions in the unsaturated zone. In the catchment subsurface, sharp reaction fronts (pyrite, carbonate) mark where vertical, unsaturated flow changes to horizontal, saturated flow, while diffuse fronts (illite, chlorite, feldspar) mark where flow is largely vertical and unsaturated.

O_2-rich interflow mixes with O_2-poor deep groundwater under the valley floor, where O_2-rich water penetrates to depths of 4 to 8 m below the water table. Oxygen oxidizes the pyrite, releasing H_2SO_4 that dissolves carbonate to create secondary porosity. This secondary porosity is hypothesized to: 1) incrementally enhance groundwater drainage from the ridgetops by increasing storage in the valley and lowering the valley water table position; 2) weaken the rock under the valley, enhancing incision. As proposed recently by Rempe and Dietrich (2014), channel incision could be the rate-limiting step that controls weathering advance beneath the watershed. However, in this shale-dominated catchment, we hypothesize that channel incision – and thus catchment geomorphological evolution – is itself enhanced by or dictated by oxidative chemical weathering under the channel.

APPENDIX 1: ATMOSPHERIC TRACERS
METHODS

Tritium concentrations were measured by helium ingrowth (Bayer and other, 1989). Water samples were degassed until <0.01% of dissolved gas remained, and were sealed in stainless steel flasks to ingrowth helium. A period of 6–12 weeks is generally sufficient to ingrow enough ^3He from the decay of ^3H ($T_{1/2} = 12.4$ yr) for analysis. Helium-3 concentrations are then measured on a MAP215-50 magnetic sector mass spectrometer using an electron multiplier to measure low abundance ^3He, which was directly correlated with the amount of tritium decayed. Tritium data were reported in tritium units (TU), where one TU was equivalent to one tritium atom per 10^{18} hydrogen atoms. Water age (τ) was then calculated from ^3He activity (^3He), tritiogenic ^3He concentrations ($^3He_{trit}$) and the ^3He decay constant ($T_{1/2}$) using the following decay function (Solomon and Sudicky, 1991):

$$\tau \frac{T_{\frac{1}{2}}}{ln2} = ln\left(\frac{[^3He_{trit}]}{^3He}\right)$$

The CFCs and SF_6 concentrations were determined on two different analytical systems using a purge-and-trap gas chromatography procedure with an electron capture detector (Busenberg and Plummer, 1992; Busenberg and Plummer, 2000). The analytical precision of these analytes were ~3% for most samples but increased near the detection limit. Detection limits were 0.0055, 0.0062, and 0.0040 picomoles/kg for CFC-11, CFC-12, and CFC-113 respectively, and was <0.01 femtomoles/kg for SF_6. Atmospheric mixing ratios, reported as parts per trillion by volume (pptv) for CFCs and SF_6 are calculated using Henry's law solubility constants as a function of recharge elevation, temperature, and salinity (compare Plummer and others, 2006). We use the average annual groundwater temperature of 9.8 °C to represent the recharge temperature and the ridgetop elevation of 300 m to represent the recharge elevation. The recharge temperature, the temperature at which water moving through the unsaturated zone entered and equili-brated with the saturated zone, was based on the average groundwater temperature variability observed in shallow the water table in the valley floor (Appendix 3), this was also the zone observed to have the greatest to response to seasonal surface temperature changes. While temperatures in the summer reach up to 14 °C, groundwater recharge predominantly occurs from November through April. The elevation of recharge was the average of the highest and lowest possible recharge areas within the region which spanned only ~100 m, as such the calculations of apparent age were insensitive to such small changes in barometric pressure associated with elevation. To estimate the recharge year for each groundwater sample, and thus residence time, the derived CFC and SF_6 values were compared to northern hemisphere atmospheric values from *ca.* 1940–present to (compare IAEA, 2006 and compiled atmospheric data therein). Given the samples were collected in 2013 and 2014, the apparent age can simply be determined as the difference the between the recharge date (indicated by the sample concentration) and the year of collection.

Estimates of groundwater age are complicated the amount of "excess air" or entrainment of air during recharge, which differs with climate (for example, annual precipitation and recharge temperature) and lithology (Busenberg and Plummer, 2000). In temperate regions receiving ~100 cm of annual precipitation excess air is typically < 1 cc L^{-1} but can reach 3 cc L^{-1} (Wilson and McNiell, 1997). More recently, Busenberg and Plummer (2014) found excess air increased with storm intensity, with values from a 17-year study in the Shenandoah National Park, Va, just ~150 miles south for SSHCZO, ranging from 0.3 to 1 cc L^{-1}. As we did not measure excess air in our samples, we provide a first cut age estimate without incorporating excess air and thus, represent the minimum ages for all samples and atmospheric tracers. Given the solubility of SF_6 is much lower than that of CFCs the incorporation of excess air during recharge has a larger effect on the estimated groundwater age from SF_6 (Goody and other, 2006). Therefore, we also used an excess air of 2 cc L^{-1} to provide an upper boundary for the SF_6 apparent ages.

RESULTS AND DISCUSSION

Tritium

Wells CZMW1 and CZMW3 had nearly identical tritium concentrations (~5.3 TU). These values are consistent with initial recharge values of 30–37 TU and a recharge age in the late 1970s and early 1980s (fig. SM1b). At shallower depths, water sampled from well CZMW2 has higher TU, which is consistent with a recharge value of 31–33 TU and a recharge age of 1985 as inferred from the history of tritium in precipitation from the region. An alternate interpretation of the tritium concentration in CZMW1-3 is that it reflects precipitation since 2000 (fig. SM1b). The water in CZMW4 has significantly less tritium than the other wells, consistent with a measurable contribution of water recharged pre-1950s.

The CFC ages are supported by comparison of tritium concentrations for the April 2013 samples. Select groundwater samples collected in April 2013 were analyzed for all water age tracers (table 3). Concentrations of CFC-12 and CFC-113 for CZMW1-3 were consistent with recharge in the late 1970s (32–35 years old). Groundwater from CZMW4 was slightly older at 36 (CFC-113) to 41 (CFC-12) years. The CFC-11 concentrations are consistent with older recharge ages.

Given that our sample indicated apparent recharge ages of approximately the 1970s-1980s, the ratio of CFC-113 and CFC-12 can provide another age estimate as CFC-113 concentrations in air increased rapidly in the late 1970s (Plummer and other, 2006). Analysis of potential mixing, assuming piston flow, and using CFC-12 and CFC-113 ratios suggests that old (CFC free) water is mixing with younger water in CZMW4 (fig. A1 A). Age estimates from the ratio of the two CFCs in CZMW4 are 31–33 years, slightly younger than, but in excellent agreement with data from the other two wells. This ratio age and mixing analysis further suggest that groundwater from CZMW4 consists nearly equal proportion of CFC free (pre-1950s) water mixing with 30–35 year old water observed in wells CZMW1 and CZMW3. Assuming the same recharge conditions (300 masl, 10 C, no salinity) and varying the amount of excess air from 1–10 cc/L results in a piston flow age of CZMW4 was 31–37 years. Increasing excess air to 20 cc/L yields a piston flow age of ~40 years.

SF_6

The April 2013 SF_6 concentrations from CZMW4 are generally consistent with CFCs and tritium results (table 3). The concentrations of SF_6 from CZMW1–3 is also in agreement with CFCs and tritium data suggested the presence of much younger water, here estimated to be approximately 9 years old at the bottom of the 15 m deep CZMW1 and 3 wells and about half that age in the 9 m deep CZMW2 well.

When an excess air of 2 cc L^{-1} was assumed for the April 2013 the apparent age the groundwater increased by 2 to 5 years, thus not altering the overall interpretation that younger water was present in CZM1&3 as compared to CZMW4. As these groundwater ages were used to estimate the rate of chlorite oxidation, we found that given an excess air of 2 cc L^{-1} increased the oxidation rate by 28%. Thus, the estimates we provide with no- excess air provide a lower boundary for chlorite oxidative weathering at SSHCZO.
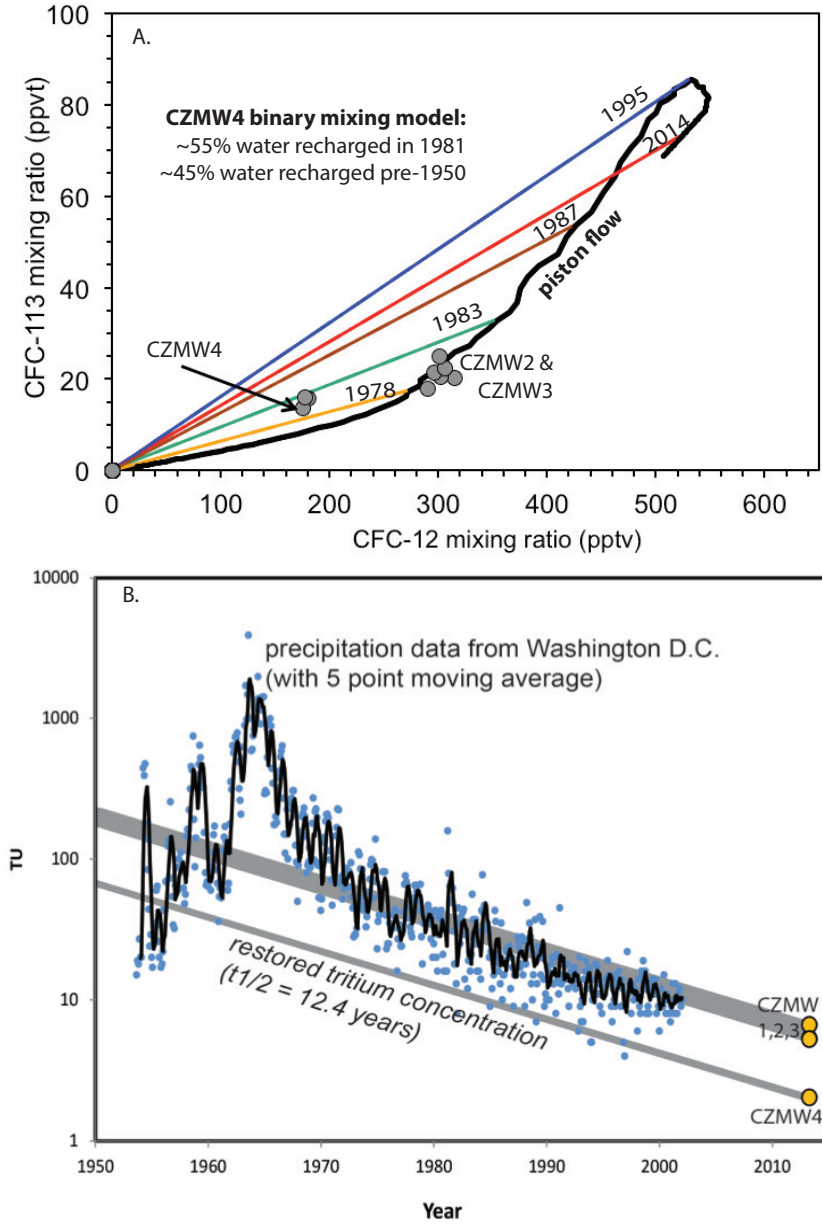
Fig. A1. (A) Piston flow model for CFC concentrations (black line). Samples from CZMW1 and CZMW3 fall on the piston flow line, thereby yielding a CFC-12/CFC-113 ratio age for recharge in the late 1970s. Sample CZMW4 is better represented by a binary mixing model of similar age water with CFC free (pre-1950s) water. (B) Comparison between tritium values measured in CZMW wells, restored to concentration at time of precipitation, and the tritium concentration in precipitation in nearby Washington D.C.

GROUNDWATER LEVELS, TEMPERATURE, CONDUCTIVITY AND PH

Table A2 1

Hydraulic head measurements at all SSHCZO well locations between December 2012 and March 2014

| Site	Water Level (m; NAVD88)											Range (m)
	12/19/12	2/28/13	4/13/13	5/23/13	6/18/13	7/10/13	8/15/l3	9/15/13	10/8/13	11/18/13	3/28/14	
well 2	260.0	260.5		260.4	260.1	260.8	259.6	259.3	259.1	259.3	260.2	1.6
well 3	259.4	259.5	259.8	259.4	259.3	259.6	259.1	258.9	259.0	259.1	259.1	0.9
well 4	261.0	260.7	261.1	260.7	260.7	260.8		260.3	2605	260.6	260.7	0.8
well 5	263.3	263.0	263.7	263.0	263.0	263.8	261.2	262.4	262.8	262.9	263.1	2.6
well 6	265.0	264.7	265.0	264.2	264.3	264.6	2623	263.6	263.9	264.9	263.6	2.7
well 7	266.7	266.7	266.6	266.5	266.5	266.5	2663	266.4	2665	266.7	266.6	0.4
well 8	267.4	267.2	267.6	267.1	267.0	267.1	264.8	265.7	265.6	266.9	267.1	2.7
well 9	273.0			273.6	273.6						273.6	0.6
well 17	258.7	258.7	258.7	258.6	258.5	258.9	258.1	258.9	257.9	258.0	258.6	1.0
well 16	280.4		280.5	280.2	280.2	280.0	280.0	279.7	279.7	279.9	280.4	0.8
well 15	282.6			282.7	281.6	282.8	282.6	282.6		282.7	182.8	0.2
well 14	279.5		279.4	278.8	279.3	278.8	278.6	278.2	278.0	278.0	279.2	1.5
well 13	273.6	273.6	273.8	273.4	272.8	273.1	273.1	272.1	272.9	273.3	273.4	1.7
well 12				275.1	275.7	275.2	275.1	275.0		275.1	275.1	0.6
well 11	270.9	270.9	271.1	270.7	270.7	270.7	269.1	269.2		270.2	270.8	2.0
well 10	270.0	269.6	270.0	269.6	269.6	269.7	267.7	267.4	267.3	269.8	269.4	2.6
DC0			277.0	276.8	276.2	277.8	276.1	275.2	275.2	275.7	278.7	2.7
CZMW8		266.0	266.3	265.9	265.7	266.1	265.2	264.9	264.9	265.2	266.3	1.4
CZMW7	293.3	293.0	293.1	293.0	293.0	293.0	293.0	291.6	291.6	293.0	293.0	1.7
CZMW6	304.8	305.0	304.6	303.8	304.0	304.3	303.6	302.0	302.0	304.7	304.8	2.9
CZMW5	294.9		295.0		295.1	295.0	294.9	294.9	294.9	295.0	0.2	
CZMW4			259.4	259.4	259.4	259.4	259.4	259.2	2592	259.3	259.4	0.2
CZMW3			260.0	259.6	259.6		259.2	259.2	259.2	259.3	260.0	0.8
CZMW2			260.3	260.0	259.7	260.1	259.6	259.2	2592	259.4	259.5	1.1
CZMW1	260.0	260.3	260.4	260.2	260.0	260.4	159.8	259.5	259.5	259.6	260.5	0.9
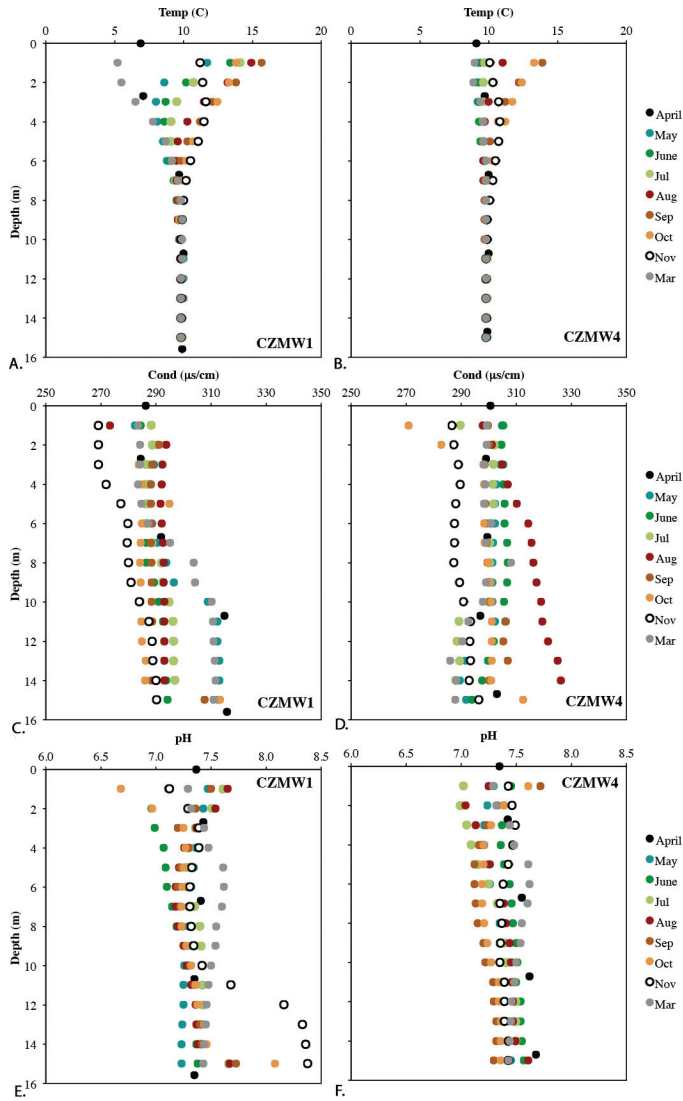
Fig. A2-1. Groundwater temperature (A and B), conductivity (C and D) and pH (E and F) observed with over time in two boreholes (CZMW1 (left) and CZMW4 (right)) lining the stream at near the watershed's outlet.
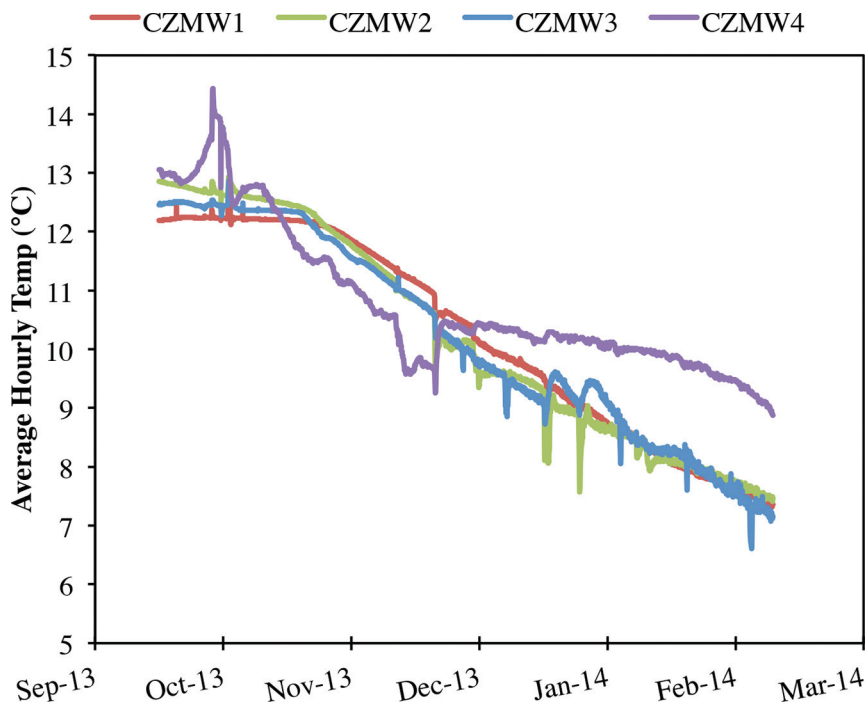
Fig. A2-2. Continuous groundwater temperature measurements from CZMW1 (red), CZMW2 (green), CZMW3 (blue), and CZMW4 (purple).

APPENDIX 3

SEM, BULK SOIL GEOCHEMISTRY AND NORMATIVE MODEL

RESULTS

Normative Model

To derive the composition of illite and chlorite we developed a normative model where we apportioned the bulk elemental composition (wt%) to known minerals utilizing the following steps: 1) all of the measured K was allocated to illite as K-feldspar concentrations were extremely low (<0.5 wt.%, by XRD), 2) Mg was then allocated to both illite and chlorite, and 3) Fe the in clay (Fe_{total} - Fe_{pyrite}) was then allocated to both illite and chlorite, here Fe^{3+} was allotted to illite over chlorite based on Fe concentrations indicated by XRD (Jin and others, 2010), mass balance and charge balance; and then Fe2+ was distributed between the two. The elemental ratios of major cations in illite and chlorite were constrained by SEM-EDS measurements (Appendix 3, tables A3-1, A3-2 and A3-3).

Comparison of Chlorite Oxidative Dissolution Rates to Erosion Rates

If the weathering advance rate is equal to the erosion rate as argued by West and others (2013), we can compare this value calculated from groundwater chemistry to the inferred long-term chlorite oxidation rate under the catchment: 20 ± 25% m My^{-1}. Over the entire 8 Ha catchment, this equates to approximately 1.2 to 2.0 m^3 of material is lost per year. Given that the concentration of chlorite in parent material is ∼ 452 mol m-3 (Jin and others, 2010), the total amount of chlorite weathered per year in the catchment lies in the range of 542–904 mol.

TABLE A3-1

SEM-EDS measurements on chlorite particles

Sample	Depth (cm)	Type	Mg/Al	Si/Al
DC9-18	549	core	0.23	NaN
DC9-18	549	core	0.30	1.08
DC9-18	549	core	0.27	0.94
DC9-50	1524	core	0.34	1.09
DC9-50	1524	core	0.30	1.00
DC9-51	1554	core	0.31	0.99
Trench_MS15	15	rock_chips	0.25	0.93
SPMS50	50	rock_chips	0.20	1.11
Trench_MS60	60	rock_chips	0.22	1.11

TABLE A3-2

SEM-EDS measurements on illite particles

Sample	Depth (cm)	Type	Mg/Al	Si/Al	K/Al	Sample	Depth (cm)	type	Mg/Al	Si/Al	K/Al
DC9-18	549	core	0.09	NaN	0.27	Trench_MS60	60	rock_chips	0.07	1.31	0.25
DC9-18	549	core	0.08	1.34	0.28	Trench_MS60	60	rock_chips	0.10	1.39	0.29
DC9-18	549	core	0.09	1.26	0.29	Trench_MS60	60	rock_chips	0.06	1.21	0.29
DC9-21	640	core	0.08	1.33	0.33	Trench_MS60	60	rock_chips	0.04	1.16	0.30
DC9-21	640	core	0.09	NaN	0.31	Trench_MS60	60	rock_chips	0.09	1.19	0.24
DC9-50	1524	core	0.07	NaN	0.33	Trench_MS100-no	100	rock_chips	0.08	1.32	0.26
DC9-50	1524	core	0.08	1.20	0.29	Trench_MS100-no	100	rock_chips	0.08	NaN	0.21
DC9-50	1524	core	0.11	1.31	0.26	Trench_MS100-no	100	rock_chips	0.07	NaN	0.29
DC9-50	1524	core	0.08	1.32	0.27	Trench_MS100-no	100	rock_chips	0.09	1.43	0.23
DC9-51	1554	core	0.09	1.40	0.27	Trench_MS100-no	100	rock_chips	0.10	NaN	0.24
DC9-51	1554	core	0.08	1.39	0.33	Trench_MS123-root	123	rock_chips	0.10	1.37	0.27
DC9-78	2377	core	0.10	1.40	0.32	Trench_MS123-root	123	rock_chips	0.09	1.33	0.25
RT-3_soil	25	Soil	0.03	1.01	0.12	Trench_RT32	32	rock_chips	0.06	NaN	0.29
RT-3_soil	25	Soil	0.08	1.12	0.09	Trench_RT32	32	rock_chips	0.08	1.42	0.26
RT-3_soil	25	Soil	0.07	1.54	0.13	Trench_RT32	32	rock_chips	0.05	1.21	0.24
RT-3_soil	25	Soil	0.05	1.15	0.15	Trench_RT32	32	rock_chips	0.08	1.31	0.25
RT-3_soil	25	Soil	0.10	1.26	0.28	Trench_RT102-root	102	rock_chips	0.03	1.29	0.32
RT-3_soil	25	Soil	0.11	1.31	0.26	Trench_RT102-root	102	rock_chips	0.06	1.39	0.29
RT-3_soil	25	Soil	0.06	1.06	0.19	Trench_RT102-root	102	rock_chips	0.08	1.29	0.27
RT-3_soil	25	Soil	0.10	1.28	0.08	Trench_RT102-root	102	rock_chips	0.05	1.24	0.33
RT-3_soil	25	Soil	0.05	1.20	0.12	Trench_RT102-root	102	rock_chips	0.10	1.34	0.29
RT-3_soil	25	Soil	0.08	1.16	0.11	Trench_RT102-root	102	rock_chips	0.08	1.33	0.32
RT-3_soil	25	Soil	0.04	1.12	0.19	Trench_RT102-root	102	rock_chips	0.05	1.42	0.31
						Trench_RT130-no	130	rock_chips	0.09	NaN	0.27
						Trench_RT130-no	130	rock_chips	0.06	1.34	0.26
						Trench_RT130-no	130	rock_chips	0.06	NaN	0.27
						SPMS50	50	rock_chips	0.05	1.20	0.32
						SPMS50	50	rock_chips	0.06	1.39	0.28

Normalized concentration of major cations determined by SEM-EDS on chlorite and illite and by ICP-AES on bulk sample

Methods	Fe/Al	Fe^{2+}/Al	K/Al	Mg/Al	Si/Al
Chlorite (SEM-EDS)	-	-	-	0.301 ± 0.026	1.019 ± 0.064
Illite (SEM-EDS)	-	-	0.281 ± 0.030	0.076 ± 0.018	1.317 ± 0.076
Bulk chemistry (deep core)	0.254 ± 0.026	0.218 ± 0.024	0.255 ± 0.010	0.129 ± 0.011	-
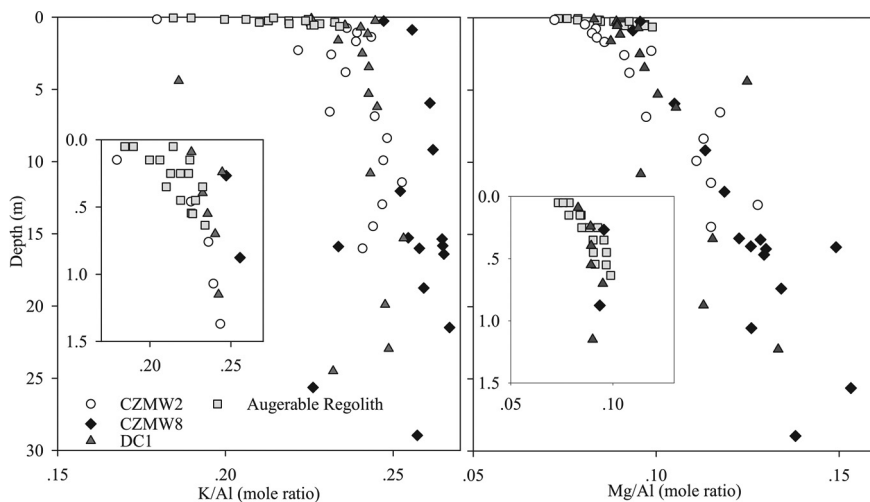
Fig. A3-1. The ratio of K to Al with depth for the soils (ridge top, mid-slope, toe slope and valley floor) and from boreholes DC1, CZMW2 and CZMW8.

REFERENCES

Anderson, S. P., Dietrich, W. E., and Brimhall, G. H., Jr., 2002, Weathering profiles, mass balance analysis, and rates of solute loss: Linkages between weathering and erosion in a small, steep catchment: Geological Society of America Bulletin, v. 114, n. 9, p. 1143–1158, http://dx.doi.org/10.1130/0016-7606(2002)1142.0.CO;2

Ayraud, V., Aquilina, L., Pauwels, H., Labasque, T., Pierson-Wickmann, A. C., Aquilina, A. M., and Gallat, G., 2006, Physical, biogeochemical and isotopic processes related to heterogeneity of a shallow crystalline rock aquifer: Biogeochemistry, v. 81, n. 3, p. 331–347.

Ayraud, V., Aquilina, L., Labasque, T., Pauwels, H., Molenat, J., Pierson-Wickmann, A. C., Durand, V., Bour, O., Tarits, C., Le Corre, P., Fourre, E., Merot, P., and Davy, P., 2008, Compartmentalization of physical and chemical properties in hard-rock aquifers deduced from chemical and groundwater age analyses: Applied Geochemistry, v. 23, n. 9, p. 2686–2707, http://dx.doi.org/10.1016/j.apgeochem.2008.06.001

Bain, C. D., 1977, The weathering of chloritic minerals in some Scottish soils: Journal of Soil Science, v. 28, n. 1, p. 144–164, http://dx.doi.org/10.1111/j.1365-2389.1977.tb02303.x

Bao, C., Shi, Y., Sullivan, P. L., Duffy, C., and Brantley, S. L., 2016, RT-Flux-PIHM: A Hydrogeochemical Model at the Watershed Scale: Water Resources Research.

Bayer, R., Schlosser, P., Bonisch, G., Rupp, H., Zaucker, F., and Zimmek, G., 1989, Performance and blank components of mass spectro-meteric systems for routine measurement of helium isotopes and tritium by 3H in-growth method: Berlin, Springer Verlag, p. 1–42.

Bern, C. R., Chadwick, O. A., Hartshorn, A. S., Khomo, L. M., and Chorover, J., 2011, A mass-balance model to separate and quantify colloidal and solute redistributions in soil: Chemical Geology, v. 282, n. 3–4, p. 113–119, http://dx.doi.org/10.1016/j.chemgeo.2011.01.014

Bern, C. R., Thompson, A., and Chadwick, O. A., 2015, Quantification of colloidal and aqueous element transfer in soils: The dual-phase mass balance model: Geochimica et Cosmochimica Acta, v. 151 p. 1–18, http://dx.doi.org/10.1016/j.gca.2014.12.008

Bethke, C. M., and Johnson, T. M., 2002, Paradox of groundwater age: Correction: Geology, v. 30, n. 4, p. 385–388, http://dx.doi.org/10.1130/0091-7613(2002)030<0386:POGAC>2.0.CO;2

––––––– 2008, Groundwater age and groundwater age dating: Annual Review of Earth and Planetary Sciences, v. 36, p. 121–152, http://dx.doi.org/10.1146/annurev.earth.36.031207.124210

Bishop, K. H., Grip, H., and O'Neill, A., 1990, The origins of acid runoff in a hillslope during storm events: Journal of Hydrology, v. 116, n. 1–4, p. 35–61, http://dx.doi.org/10.1016/0022-1694(90)90114-D

Bishop, K., Seibert, J., Köhler, S., and Laudon, H., 2004, Resolving the double paradox of rapidly mobilized old water with highly variable responses in runoff chemistry: Hydrological Processes, v. 18, n. 1, p. 185–189, http://dx.doi.org/10.1002/hyp.5209

Böhlke, J. K., and Denver, J. M., 1995, Combined use of groundwater dating, chemical, and isotopic analyses to resolve the history and fate of nitrate contamination in two agricultural watersheds, Atlantic coastal plain, Maryland: Water Resources Research, v. 31, n. 9, p. 2319–2339, http://dx.doi.org/10.1029/95WR01584

Böhlke, J. K., Wanty, R., Tuttle, M., Delin, G., and Landon, M., 2002, Denitrification in the recharge area and discharge area of a transient agricultural nitrate plume in a glacial outwash sand aquifer, Minnesota: Water Resources Research, v. 38, n. 7, p. 10-1–10-26, http://dx.doi.org/10.1029/2001WR000663

Bonnissel-Gissinger, P., Alnot, M., Ehrhardt, J. J., and Behra, P., 1998, Surface oxidation of pyrite as a function of pH: Environmental Science & Technology, v. 32, n. 19, p. 2839–2845, http://dx.doi.org/10.1021/es980213c

Brantley, S. L., 2008, Chapter 5, Kinetics of Mineral Dissolution, *in* Brantley, S. L., Kubicki, J. D., and White, A. F., editors, Kinetics of Water-Rock Interaction: New York, Springer, p. 151–210, http://dx.doi.org/10.1007/978-0-387-73563-4_5

Brantley, S. L., and Lebedeva, M., 2011, Learning to read the chemistry of regolith to understand the critical zone: Annual Review of Earth and Planetary Sciences, v. 39, p. 387–416, http://dx.doi.org/10.1146/annurev-earth-040809-152321

Brantley, S. L., and White, A. F., 2009, Approaches to modeling weathered regolith: Reviews in Mineralogy and Geochemistry, v. 70, p. 435–484, http://dx.doi.org/10.2138/rmg.2009.70.10

Brantley, S. L., Goldhaber, M. B., and Ragnarsdottir, K. V., 2007, Crossing disciplines and scales to understand the critical zone: Elements, v. 3, n. 5, p. 307–314, http://dx.doi.org/10.2113/gselements.3.5.307

Brantley, S. L., Buss, H., Lebedeva, M., Fletcher, R. C., and Ma, L., 2011, Investigating the complex interface where bedrock transforms to regolith: Applied Geochemistry, v. 26, Supplement, p. S12–S15, http://dx.doi.org/10.1016/j.apgeochem.2011.03.017

Brantley, S. L., Holleran, M. W., Jin, L., and Basilevskaya, E., 2013, Probing deep weathering in the Shale Hills Critical Zone Observatory, Pennsylvania (USA): The hypothesis of nested chemical reaction fronts in the subsurface: Earth Surface Processes and Landforms, v. 38, n. 11, p. 1280–1298, http://dx.doi.org/10.1002/esp.3415

Brantley, S. L., Lebedeva, M., Balashov, V., Singha, K., Sullivan, P. L., and Stinchcomb, G., 2016, Toward a conceptual model relating chemical reaction fronts to water flowpaths in hills: Geomorphology, http://dx.doi.org/10.1016/j.geomorph.2016.09.027

Brimhall, G., and Dietrich, W. E., 1987, Constitutive mass balance relations between chemical composition, volume, density, porosity, and strain in metasomatic hydrochemical systems: Results on weathering and pedogenisis: Geochimica et Cosmochimica Acta, v. 51, n. 3, p. 567–587, http://dx.doi.org/10.1016/0016-7037(87)90070-6

Busenberg, E., and Plummer, L. N., 1992, Use of Chlorofluorocarbons (CCL_3F and CCL_2F_2) as Hydrologic Tracers and Age-Dating Tools: The Alluvium and Terrace System of Central Oklahoma: Water Resources Research, v. 28, n. 9, p. 2257–2283, http://dx.doi.org/10.1029/92WR01263

_____ 2000, Dating young groundwater with sulfur hexafluoride: Natural and anthropogenic sources of sulfur hexafluoride: Water Resources Research, v. 36, n. 10, p. 3011–3030, http://dx.doi.org/10.1029/2000WR900151

_____ 2008, Dating groundwater with trifluoromethyl sulfurpentafluoride (SF_5CF_3), sulfur hexafluoride (SF_6), CF_3Cl (CFC-13), and CF_2Cl_2 (CFC-12): Water Resources Research, v. 44, n. 2, http://dx.doi.org/10.1029/2007WR006150

Chigira, M., 1990, A mechanism of chemical weathering of mudstone in a mountainous area: Engineering Geology, v. 29, n. 2, p. 119–138, http://dx.doi.org/10.1016/0013-7952(90)90002-I

Chigira, M., and Oyama, T., 1999, Mechanism and effect of chemical weathering of sedimentary rocks: Engineering Geology, v. 55, n. 1–2, p. 3–14, http://dx.doi.org/10.1016/S0013-7952(99)00102-7

Clark, G. M., and Ciolkosz, E. J., 1988, Periglacial geomorphology of the Appalachian highlands and interior highlands south of the glacial border – A review: Geomorphology, v. 1, n. 3, p. 191–220, http://dx.doi.org/10.1016/0169-555X(88)90014-1

Cotter, E., and Inners, J., 1986, Silurian stratigraphy and sedimentology in the Huntingdon County area, *in* Sevon, W., editor, Guidebook for the 51st Annual Field Conference of Pennsylvania Geologists, Selected geology of Bedford and Huntingdon Counties: Field Conference of Pennsylvania Geologists, Bureau of Topographic and Geologic Survey, p. 27–39.

Dávila, P. F., Kúlls, C., and Weiler, M., 2013, A toolkit for groundwater mean residence time interpretation with gaseous tracers: Computers & Geosciences, v. 61, p. 116–125, http://dx.doi.org/10.1016/j.cageo.2013.08.006

Drake, H., Tullborg, E., and MacKenzie, A. B., 2009, Detecting the near-surface redox front in crystalline bedrock using fracture mineral distribution, geochemistry and U-series disequilibrium: Applied Geochemistry, v. 24, n. 5, p. 1023–1039, http://dx.doi.org/10.1016/j.apgeochem.2009.03.004

Feldman, C., 1983, Behavior of trace refractory minerals in the lithium metaborate fusion acid dissolution procedure: Analytical Chemistry, v. 55, n. 14, p. 2451–2453, http://dx.doi.org/10.1021/ac00264a064

Fetter, C. W., 2000, Applied Hydrogeology: Upper Saddle River, New Jersey, Prentice Hall, 598 p.

Flueckinger, L. A., 1969, Geology of a portion of the Allensville quadrangle, Centre and Huntingdon Counties, Pennsylvania, Progress Report 176: Commonwealth of Pennsylvania, State Planning Board, Bureau of Topographic and Geologic Survey.

Gilmore, T. E., Genereux, D. P., Solomon, D. K., and Solder, J. E., 2016, Groundwater transit time distribution and mean from streambed sampling in an agricultural coastal plain watershed, North Carolina, USA: Water Resources Research, v. 52, n. 3, p. 2025–2044, http://dx.doi.org/10.1002/2015WR017600

Gleeson, T., and Manning, A. H., 2008, Regional groundwater flow in mountainous terrain: Three–dimensional simulations of topographic and hydrogeologic controls: Water Resources Research, v. 44, n. 10, http://dx.doi.org/10.1029/2008WR006848

Goldich, S. S., 1984, Determination of Ferrous Iron in Silicate Rocks: Chemical Geology, v. 42, n. 1–4, p. 343–347, http://dx.doi.org/10.1016/0009-2541(84)90027-5

Goody, D. C., Darling, W. G., Abseer, C., and Lapworth, D. J., 2006, Using chlorofluorocarbons (CFCs) and sulphur hexafluoride (SF_6) to characterize groundwater movement and residence time and a lowland Chalk catchment: Journal of Hydrology, v. 330, n. 1–2, p. 44–52, http://dx.doi.org/10.1016/j.jhydrol.2006.04.011

Graham, R. C., Rossi, A. M., and Hubbert, K. R., 2010, Rock to regolith conversion: Producing hospitable substrates for terrestrial ecosystems: GSA Today, v. 20, n. 2, p. 4–9, http://dx.doi.org/10.1130/GSAT57A.1

Guo, L., Chen, J., and Lin, H., 2014, Subsurface lateral preferential flow network revealed by time–lapse ground-penetrating radar in a hillslope: Water Resources Research, v. 50, n. 12, p. 9127–9147, http://dx.doi.org/10.1002/2013WR014603

Hercod, D. J., Brady, P. V., and Gregory, R. T., 1998, Catchment-scale coupling between pyrite oxidation and calcite weathering: Chemical Geology, v. 151, n. 1–4, p. 259–276, http://dx.doi.org/10.1016/S0009-2541(98)00084-9

Herndon, E. M., Dere, A. L., Sullivan, P. L., Norris, D., Reynolds, B., and Brantley, S. L., 2015, Landscape heterogeneity drives contrasting concentrations-discharge relationships in shale headwater catchments: Hydrology and Earth System Science, v. 19, p. 3333–3347, http://dx.doi.org/10.5194/hessd-12-213-2015

Jin, L., and Brantley, S. L., 2011, Soil chemistry and shale weathering on a hillslope influenced by convergent hydrologic flow regime at the Susquehanna/Shale Hills Critical Zone Observatory: Applied Geochemistry, v. 26, Supplement, p. S51–S56, http://dx.doi.org/10.1016/j.apgeochem.2011.03.027

Jin, L., Ravella, R., Ketchum, B., Bierman, P. R., Heaney, P., White, T., and Brantley, S. L., 2010, Mineral weathering and elemental transport during hillslope evolution at the Susquehanna/Shale Hills Critical Zone Observatory: Geochimica et Cosmochimica Acta, v. 74, n. 13, p. 3669–3691, http://dx.doi.org/10.1016/j.gca.2010.03.036

Jin, L., Rother, G., Cole, D. R., Mildner, D. F. R., Duff, C. J., and Brantley, S. L., 2011, Characterization of deep weathering and nanoporosity development in shale—A neutron study: American Mineralogist, v. 96, n. 4, p. 498–512, http://dx.doi.org/10.2138/am.2011.3598

Jin, L., Ogrinc, N., Yesavage, T., Hasenmuller, E. A., Ma, L., Sullivan, P. L., Kaye, J., Duffy, C., and Brantley, S. L., 2014, The CO_2 consumption potential during gray shale weathering: Insights from the evolution of carbon isotopes in the Susquehanna Shale Hills critical zone observatory: Geochimica et Cosmochimica Acta, v. 142, p. 260–280, http://dx.doi.org/10.1016/j.gca.2014.07.006

Johnson, L. J., 1964, Occurrence of regularly interstratified chlorite-vermiculite as a weathering product of chlorite in a soil: American Mineralogist, v. 49, n. 5–6, p. 556–572.

Jones, J. B. J., Jr., and Isaac, R. A., 1972, Determination of sulfur in plant material using a Leco Sulfur

Analyzer: Journal of Agricultural and Food Chemistry, v. 20, n. 6, p. 1292–1294, http://dx.doi.org/10.1021/jf60184a027

Kennedy, C. D., Genereux, D. P., Corbett, D. R., and Mitasova, H., 2009, Relationships among groundwater age, denitrification, and the coupled groundwater and nitrogen fluxes through a streambed: Water Resources Research, v. 45, n. 9, http://dx.doi.org/10.1029/2008wr007400

Kuntz, B. W., Rubin, S., Berkowitz, B., and Singha, K., 2011, Quantifying solute transport at the Shale Hills Critical Zone Observatory: Vadose Zone Journal, v. 10, n. 3, p. 843–857, http://dx.doi.org/10.2136/vzj2010.0130

Lebedeva, M. I., Fletcher, R. C., Balashov, V. N., and Brantley, S. L., 2007, A reactive diffusion model describing transformation of bedrock to saprolite: Chemical Geology, v. 244, n. 3–4, p. 624–645, http://dx.doi.org/10.1016/j.chemgeo.2007.07.008

Lebedeva, M. I., Fletcher, R. C., and Brantley, S. L., 2010, A mathematical model for steady-state regolith production at constant erosion rate: Earth Surface Processes and Landforms, v. 35, n. 5, p. 508–524, http://dx.doi.org/10.1002/esp.1954

Lee, B. D., Sears, S. K., Graham, R. C., Amrhein, C., and Vali, H., 2003, Secondary mineral genesis from chlorite and serpentine in an ultramafic soil toposequence: Soil Science Society of America Journal, v. 67, n. 4, p. 1309–1317, http://dx.doi.org/10.2136/sssaj2003.1309

Lin, H., and Zhou, X., 2008, Evidence of subsurface preferential flow using soil hydrologic monitoring at the Shale Hills catchment: European Journal of Soil Science, v. 59, n. 1, p. 34–49, http://dx.doi.org/10.1111/j.1365-2389.2007.00988.x

Lin, H. S., Kogelmann, W., Walker, C., and Bruns, M. A., 2006, Soil moisture patterns in a forested catchment: A hydropedological perspective: Geoderma, v. 131, n. 3–4, p. 345–368, http://dx.doi.org/10.1016/j.geoderma.2005.03.013

Lichtner, P. C., 1988, The quasi-stationary state approximation to coupled mass transport and fluid-rock interaction in a porous medium: Geochimica et Cosmochimica Acta, v. 52, n. 1, p. 143–65, http://dx.doi.org/10.1016/0016-7037(88)90063-4

Ma, L., Chabaux, F., West, N., Kirby, E., Jin, L., and Brantley, S., 2013, Regolith production and transport in the Susquehanna Shale Hills Critical Zone Observatory, Part 1: Insights from U-series isotopes: Journal of Geophysical Research: Earth Surface, v. 118, n. 2, p. 722–740, http://dx.doi.org/10.1002/jgrf.20037

Maher, K., 2010, The dependence of chemical weathering rates on fluid residence time: Earth and Planetary Science Letters, v. 294, n. 1–2, p. 101–110, http://dx.doi.org/10.1016/j.epsl.2010.03.010

—————— 2011, The role of fluid residence time and topographic scales in determining chemical fluxes from landscapes: Earth and Planetary Science Letters, v. 312, n. 1–2, p. 48–58, http://dx.doi.org/10.1016/j.epsl.2011.09.040

Manning, A. H., and Caine, J. S., 2007, Groundwater noble gas, age, and temperature signatures in an Alpine watershed: Valuable tools in conceptual model development: Water Resources Research, v. 43, n. 4, http://dx.doi.org/10.1029/2006WR005349

Manning, A. H., Clark, J. F., Diaz, S. H., Rademacher, L. K., Earman S., and Plummer, L. N., 2012, Evolution of groundwater age in a mountain watershed over a period of thirteen years: Journal of Hydrology, v. 460–461, p. 13–28, http://dx.doi.org/10.1016/j.jhydrol.2012.06.030

Manning, A. H., Verplanck, P. L., Caine, J. S., and Todd, A. S., 2013, Links between climate change, water-table depth, and water chemistry in a mineralized mountain watershed: Applied Geochemistry, v. 37, p. 64–87, http://dx.doi.org/10.1016/j.apgeochem.2013.07.002

Meek, K., Derry, L., Sparks, J., and Cathles, L., 2016, $^{87}Sr/^{86}Sr$, Ca/Sr, and Ge/Si ratios as tracers of solute sources and biogeochemical cycling at a temperate Forested shale catchment, central Pennsylvania, USA: Chemical Geology, http://dx.doi.org/10.1016/j.chemgeo.2016.04.026

Modica, E., Buxton, H. T., and Plummer, L. N., 1998, Evaluating the source and residence times of groundwater seepage to streams, New Jersey Coastal Plain: Water Resources Research, v. 34, n. 11, p. 2797–2810.

Molnar, P., Anderson, R. S. and Anderson, S. P., 2007, Tectonics, fracturing of rock, and erosion: Journal of Geophysical Research, v. 112, p. 1–12. doi:10.11029/12005JF000433,002007.

Moses, C. O., and Herman, J. S., 1991, Pyrite oxidation at circumneutral pH: Geochimica et Cosmochimica Acta, v. 55, n. 2, p. 471–482, http://dx.doi.org/10.1016/0016-7037(91)90005-P

Noireaux, J., Gaillardet, J., Sullivan, P. L., and Brantley, S. L., 2014, Boron isotope fractionation in soils at Shale Hills CZO: Procedia Earth and Planetary Sciences, v. 10, p. 218–222, http://dx.doi.org/10.1016/j.proeps.2014.08.024

Parkhurst, P. L., and Appelo, C. A. J., 1999, User's guide to PHREEQC (version 2)– a computer program for speciation, batch-reaction, one-dimensional transport, and inverse geochemical calculations: US Geological Survey Water-Resources Investigations Report 99-4259, 738 p.

Plummer, L. N., Busenberg, E., and Cook, P. G., 2006, Chapter 3, Principles of Chlorofluorocarbon dating *in* Use of Chlorofluorocarbons in Hydrology: A Guidebook: Vienna, Austria, International Atomic Energy Agency, p. 17–29

Proust, D., Eymery, J. P., and Beaufort, D., 1986, Supergene vermiculitization of a magnesian chlorite: Iron and magnesium removal processes: Clays and Clay Minerals, v. 34, n. 5, p. 572–580.

Rempe, D. M., and Dietrich, W. E., 2014, A bottom-up control on fresh-bedrock topography under landscapes: Proceedings of the National Academy of Sciences of the United States of America, v. 111, n. 18, p. 6576–6581, http://dx.doi.org/10.1073/pnas.1404763111

Ross, G. J., Wang, C., Ozkan, A. L., and Rees, H. W., 1982, Weathering of chlorite and mica in a New Brunswick podzol developed on till derived from chlorite-mica schist: Geoderma, v. 27, n. 3, p. 255–267, http://dx.doi.org/10.1016/0016-7061(82)90034-9

Sebol, L. A., Robertson, W. D., Busenberg, E., Plummer, L. N., Ryan, M. C., and Schiff, S. L., 2007, Evidence

of CFC degradation in groundwater under pyrite-oxidizing conditions: Journal of Hydrology, v. 347, n. 1–2, p. 1–12, http://dx.doi.org/10.1016/j.jhydrol.2007.08.009

Singh, R. N., Grube, W. E., Smith, R. M., and Keefer, R. F., 1982, Relation of pyritic sandstone weathering to soil and minesoil properties, *in* Kittrick, J. A., Fanning, D. S., and Hossner, L. R., editors, Acid Sulfate Weathering: Madison, Wisconsin, Soil Science Society of America, SSSA Special Publication 10, p. 193–208, http://dx.doi.org/10.2136/sssaspecpub10.c11

Strumm, W., 1997, Reactivity at the mineral-water interface: Dissolution and inhibition: Colloid and Surfaces A: Physiochemical and Engineering Aspects, v. 120, n. 1–3, p. 143–166, http://dx.doi.org/10.1016/S0927-7757(96)03866-6

Sullivan, P. L., Ma, L., West, N., Jin, L., Karwan, D. K., Noireaux, J., Steinhoefel, G., Gaines, K. P., Eissenstat, D. M., Gaillardet, J., Derry, L. A., Meek, K., Hynek, S., and Brantley, S. L., 2016, CZ-tope at Susquehanna Shale Hills CZO: Synthesizing multiple isotope proxies to elucidate Critical Zone processes across timescales in a temperate forested landscape: Chemical Geology, http://dx.doi.org/10.1016/j.chemgeo.2016.05.012

Thomas, E. M., Lin, H., Duffy, C. J., Sullivan, P. L., Holmes, G. H., Brantley, S. L., and Jin, L., 2013, Spatiotemporal patterns of water stable isotope compositions at the Shale Hills Critical Zone Observatory: Linkages to Subsurface Hydrologic Processes: Vadose Zone Research, v. 12, n. 4, http://10.2136/vzj2013.01.0029.01.0029

West, N., Kirby, E., Bierman, P., Slingerland, R., Ma, L., Rood, D., and Brantley, S. L., 2013, Regolith production and transport at the Susquehanna Shale Hills Critical Zone Observatory, Part 2: Insights from meteoric [10]Be: Journal of Geophysical Research: Earth Surface, v. 118, p. 1877–1896, http://10.213610.1002/jgrf.20121

West, N., Kirby, E., Bierman, P., and Clarke, B. A., 2014, Aspect-dependent variations in regolith creep revealed by meteoric [10]Be: Geology, v. 42, n. 6, p. 507–510, http://dx.doi.org/10.1130/g35357.1

White, A. F., and Brantley, S. L., 1995, Chemical weathering rates of silicate minerals: An overview, *in* White, A. F., and Brantley, S. L., editors, Chemical Weathering Rates of Silicate Minerals: Reviews in Mineralogy and Geochemistry, v. 31, p. 1–22.

Williams, J. H., and Johnson, C. D., 2004, Acoustic and optical borehole-wall imaging for fractured-rock aquifer studies: Journal of Applied Geophysics, v. 55, n. 1–2, p. 151–159, http://dx.doi.org/10.1016/j.jappgeo.2003.06.009

Wilson, G. B., and McNeill, G. W., 1997, Noble gas recharge temperatures and excess air component: Applied Geochemistry, v. 12, n. 6, p. 747–762, http://dx.doi.org/10.1016/S0883-2927(97)00035-8

Yesavage, T., Fantle, M. S., Vervoort, J., Mathur, R., Jin, L., Liermann, L. J., and Brantley, S. L., 2012, Fe cycling in the Shale Hills Critical Zone Observatory, Pennsylvania: An analysis of biogeochemical weathering and Fe isotope fractionation: Geochimica et Cosmochimica Acta, v. 99, p. 18–38, http://dx.doi.org/10.1016/j.gca.2012.09.029

Zhang, J., Lin, H., and Doolittle, J., 2014, Soil layering and preferential flow impacts on seasonal changes of GPR signals in two contrasting soils: Geoderma, v. 213, p. 560–569, http://dx.doi.org/10.1016/j.geoderma.2013.08.035